Quantification of morphological, functional, and biochemical features of H9c2 rat cardiomyoblast retinoic acid differentiation

Nicole S. York[1*], Joel E. Rivera[1], Mohammadreza Rahmani Manesh[1], K'sana Wood Lynes-Ford[1,2], Rory Smith[1], Leigh E. Wicki-Stordeur[1], Laura T. Arbour[1,2,3], Leigh Anne Swayne[1,3*]

(1) Division of Medical Sciences, University of Victoria, Victoria, British Columbia, Canada
(2) Department of Medical Genetics, University of British Columbia, Victoria, British Columbia, Canada
(3) Island Medical Program, University of British Columbia, Victoria, British Columbia, Canada

(*) Correspondence should be addressed to Leigh Anne Swayne, lswayne@uvic.ca or to Nicole York, nicoleyork@uvic.ca.

Running Head: Quantification of H9c2 cell differentiation

Abbreviations:

iPSC	induced pluripotent stem cell
$Ca_v1.2$	protein pore subunit of the of the L-type calcium channel encoded by the *CACNA1C* gene
Ca^{2+}	Calcium ions
$[Ca^{2+}]_i$	Internal calcium ion concentration
STED	Stimulated emission depletion
NaCl	Sodium chloride
E15.5	Embryonic Day 15.5
P2	Postnatal Day 2
DMEM	Dulbecco's Modified Eagle Medium
FBS	Fetal bovine serum
RIPA	Radio-Immunoprecipitation Assay
BDM	2,3-Butanedione monoxime
HBSS	Hanks' Balanced Salt Solution
dPBS	Dulbecco's Phosphate-Buffered Saline
Sqrt	Square root
FOV	field of view
FC	fold change
TBS	Tris-buffered saline
TBS-T	Tris-buffered saline, 0.1% Tween-20

Abstract

Cell culture models enable advancement in our understanding of heart development and heart disease. The H9c2 rat ventricular cardiomyoblast cell line can be differentiated, recapitulating certain components of cardiomyocyte development; however, morphological, functional, and biochemical changes are rarely investigated in parallel, thereby limiting fulsome understanding. We therefore characterized morphology, Ca^{2+} handling, and gene expression after five days (5 *days-in-vitro*, DIV5), and fourteen days (DIV14) of exposure to differentiation stimuli, consisting of retinoic acid and low serum. Subpopulations of cells showed evidence of differentiation to a cardiomyocyte-like phenotype that was enhanced over time. Differentiation was also associated with the formation of cytoplasmic actin clusters. Spontaneous Ca^{2+} transients in differentiated H9c2 cells had decreased frequency and synchronicity compared to those observed in primary cardiomyocytes. Additionally, key cardiomyocyte cytoskeletal proteins and ion channel transcript and protein expression levels changed significantly with differentiation, in alignment with changes normally observed in cardiomyocyte development. Our findings suggest H9c2 cells may be used as a high throughput screening model to investigate cardiomyocyte biology in certain developmental contexts with relevance to heart health and disease.

Significance statement

- Retinoic acid-differentiated rat ventricular H9c2-cardiomyoblast cells model aspects of cardiomyocyte development with quick turnover rates and potentially relatively high homogeneity compared to other common cell culture

models. Characterizing morphology, Ca^{2+} handling, and gene expression changes will help experimental design and contextualizing outcomes.

- Subsets of differentiated H9c2 cells exhibit morphology changes consistent with a cardiomyocyte-like phenotype, Ca^{2+} signaling, and gene expression changes.
- These outcomes suggest H9c2 responses to differentiation increase over time and are somewhat heterogenous as only sub-populations appear to respond. These findings provide insight for designing cardiomyocyte development studies using H9c2 cells in healthy and disease state contexts.

Introduction

Cardiomyocyte-like cell culture models, including immortalized cell lines such as H9c2 rat cardiomyoblasts, human induced pluripotent stem cell (iPSC)-derived cardiomyocytes, and rodent primary cardiomyocyte cultures (Figure 1) play key, complementary roles in modeling cardiomyocyte development. Together, their coordinated use could enable fulsome modelling of the cellular changes in health and disease contexts. Each of these models has key strengths and weaknesses facilitating the study of different aspects of cardiomyocyte development and viability. Here we focused on building a comprehensive view of the H9c2 cell line in the context of retinoic acid differentiation as a developmental model, from morphological, functional, and biochemical perspectives.

H9c2 cells are touted as having ‘cardiac’ (vs skeletal) muscle features and quick, easy, and maintainable culturing protocols (Figure 1). The H9c2 cell line was first isolated from the lower half of a rat heart at embryonic day 13 (Kimes and Brandt, 1976). Following

66 selective passage to enrich for cardiomyoblasts, the cells ceased beating but maintained
67 other key cardiomyoblast characteristics (Kimes and Brandt, 1976), such as their
68 morphology, ultrastructure, and presence of specific ion channels (Kimes and Brandt,
69 1976; Hescheler *et al.*, 1991; Ménard *et al.*, 1999; Watkins *et al.*, 2011). Exposing H9c2
70 cells to low serum and all trans retinoic acid increased expression of Cav1.2 (then known
71 as α_{1C})-based L-type Ca^{2+} channels (Ménard *et al.*, 1999), which are enriched in and
72 important for generating the electrical and mechanical properties of cardiomyocytes
73 (Harvey and Hell, 2013), and cardiac troponins (Branco *et al.*, 2015), suggesting that these
74 stimuli drove the cells towards a cardiac phenotype. Together this work positioned H9c2
75 cells as a cell line model for cardiomyoblast development.
76 Several studies have investigated the morphological and biochemical aspects of
77 differentiating H9c2 cells (Branco *et al.*, 2015; Kankeu *et al.*, 2018), but rarely have these
78 been integrated, and functional studies are rare (Ménard *et al.*, 1999; Campero-Basaldua
79 *et al.*, 2023). In terms of morphology, H9c2 cell differentiation is associated, albeit mainly
80 qualitatively, with elongation of cell shape (Ménard *et al.*, 1999; Branco *et al.*, 2015;
81 Kankeu *et al.*, 2018; Campero-Basaldua *et al.*, 2023). In different disease modeling
82 contexts, H9c2 cells exhibit morphological changes at the cellular and subcellular levels,
83 including cell shrinkage (Sardão *et al.*, 2009; Lekes *et al.*, 2016), membrane blebbing and
84 narrowing (Sardão *et al.*, 2009), as well as changes to the actin stress fiber and myosin
85 distribution (Sardão *et al.*, 2009; Varela *et al.*, 2021); however, morphological changes
86 during differentiation have been quantified to this extent. To date, characterization of
87 intracellular Ca^{2+} dynamics has been mainly limited to undifferentiated H9c2 cells

88 (Avanzato *et al.*, 2014; Xu *et al.*, 2020), and/or conditions of pharmacologically evoked
89 activity (Campero-Basaldua *et al.*, 2023). These studies show that treatments with NaHS
90 (Avanzato *et al.*, 2014), glucose (Xu *et al.*, 2020), and caffeine and vasopressin (Campero-
91 Basaldua *et al.*, 2023), influence Ca^{2+} dynamics, underscoring the importance of carefully
92 considering differentiation state and experimental conditions when using this cell line as a
93 model.

94 In contrast to this relative rich literature on Ca^{2+} dynamics in undifferentiated H9c2
95 cells, little is known regarding Ca^{2+} transient profiles across H9c2 cell differentiation. In
96 contrast to studies on morphology and function, gene expression changes in H9c2 cell
97 differentiation have been more thoroughly examined (Branco *et al.*, 2015; Kankeu *et al.*,
98 2018; Campero-Basaldua *et al.*, 2023); however, these were rarely examined in
99 conjunction with the morphological and/or functional aspects of differentiation. H9c2 cell
100 differentiation is associated with increased expression of genes encoding cardiomyocyte
101 markers, such as cardiac troponins, and genes involved in Ca^{2+} handling and mitochondrial
102 metabolism (Branco *et al.*, 2015)**.** How these gene expression changes link to
103 morphological and/or functional changes, such as changes in Ca^{2+} handling, are unknown.

104 In the current study, we sought to bridge the gap in knowledge of integrated
105 understanding of morphological, functional, and biochemical changes across H9c2 cell
106 retinoic acid differentiation. We performed confocal and super-resolution microscopy,
107 intracellular Ca^{2+} imaging, and RT-qPCR and Western blotting to analyze H9c2 cell
108 morphology, function, and biochemical changes, respectively. Differentiated H9c2 cell
109 populations had increased length, perimeter, area, and number of nuclei and displayed

110 changes in subcellular actin structures. Spontaneous Ca^{2+} dynamics of differentiated
111 H9c2 cells were decreased compared to those observed in primary cardiomyocytes,
112 suggesting retinoic acid differentiation drives functional cardiomyocyte development to a
113 lesser extent as seen in other models. We also observed significant gene expression
114 changes consistent with cardiomyocyte differentiation. In summary, here we provide a
115 detailed quantitative analysis of morphology, function, and gene expression of H9c2 cells
116 across differentiation that will facilitate their use as an experimental model for
117 cardiomyocyte development.
118

119 **Results**

120 **Subpopulations of differentiated H9c2 cells exhibits changes in gross morphology and**
121 **contain specialized subcellular actin structures**

122 During cardiomyocyte differentiation, cells undergo changes in their overall shape
123 that are key for their function (Hirschy *et al.*, 2006; Ahuja *et al.*, 2007; Lundy *et al.*, 2013).
124 Prior work commonly differentiated up to DIV5 (e.g. Branco *et al.*, 2015; Kankeu *et al.*,
125 2018), yet more recent work has extended differentiation to DIV14 (Campero-Basaldua *et*
126 *al.*, 2023). We therefore quantified gross morphological changes from two cohorts of cells:
127 DIV0 vs. DIV5 (Figure 2 A, B), and DIV5 vs. DIV14 (Figure 2 M, N). Using a custom MATLAB
128 script, we measured cell length, perimeter, area, eccentricity, and the number of nuclei
129 per cell from confocal micrographs of H9c2 cells labelled for F-actin (phalloidin) and
130 nuclei (Hoechst). There were no significant changes in the overall mean gross morphology
131 data between DIV0 and DIV5 (Figure 2 C-G). However, we noted a right shift in the

132 frequency distribution plot of cell length for DIV5 (Figure 2 H). Similar right shifts were
133 observed for the frequency distributions of perimeter (Figure 2 I), cell area (Figure 2 J), and
134 number of nuclei per cell (Figure 2 L). Together these shifts indicate that subpopulation(s)
135 of DIV5 cells are longer, larger, and contain more nuclei than those at DIV0 suggesting that
136 a subpopulation of DIV5 cells exhibits a phenotype that is in the process of differentiating
137 to a cardiomyocyte-like phenotype for length, perimeter, area, and number of nuclei.
138 Similarly, there were no significant changes in the mean values of the gross morphology
139 metrics between DIV5 and DIV14 cells (Figure 2 O-S). Yet, we observed a right shift in the
140 frequency distribution plots of perimeter (Figure 2 U), area (Figure 2 V), and number of
141 nuclei (Figure 2 X) at DIV14, suggesting that differentiation increased the subpopulations of
142 cells that were longer, larger, and with more nuclei and that extending the time in
143 differentiation conditions further enhances the cardiomyocyte-like phenotypic changes.
144 Notably, we found that DIV14 differentiated H9c2 cells commonly exhibited
145 saturated coils, or "clusters" of F-actin (phalloidin+) (Figure 2 N) like those previously
146 reported in other cell types (Fritzsche *et al.*, 2017; Shirai *et al.*, 2017; Carton *et al.*, 2023).
147 We used stimulated emission depletion (STED) super-resolution microscopy to further
148 resolve these F-actin clusters. Many of these clusters were circular (Figure 3 A-C) to
149 ellipsoid (Figure 3 D) in nature. At DIV14, 61.8% ± 5.1 of cells showed actin clusters
150 compared to 10.8% ± 2.0 of cells at DIV5 (Welch's t-test, p=0.0072; Figure 3 E). Among the
151 cells that exhibited actin clusters, the average number of clusters per cell increased
152 between these time points. At DIV5, cells contained 1.0 ± 0.1 clusters per cell, while at
153 DIV14, this increased to 2.7 ± 0.3 clusters per cell (Welch's t-test, p=0.0048; Figure 3 F).

154 Together these results suggest that retinoic acid differentiation increases cell
155 length, cell area, and the number of nuclei per cell and induces the formation of
156 circular/elliptical F-actin clusters.
157
158 **Subpopulation of H9c2 cell spontaneous Ca^{2+} transients approach the frequencies**
159 **and synchronicities commonly observed in primary cardiomyocytes**
160 Ca^{2+} signalling underlies cardiomyocyte contraction and is modulated across the
161 development of cardiomyoblasts into cardiomyocytes (Louch *et al.*, 2015). Yet, putative
162 changes in H9c2 cell intracellular Ca^{2+} dynamics across differentiation remain largely
163 unexplored. In initial studies we found it difficult to reliably detect readily quantifiable Ca^{2+}
164 transients in undifferentiated H9c2 cells. Therefore, we used confocal live-cell imaging of
165 Fluo4-AM (Gee *et al.*, 2000) to quantify spontaneous Ca^{2+} transients in DIV5 and DIV14
166 differentiated H9c2 cells (Figure 4 A, B). We further measured Ca^{2+} transients in neonatal
167 primary mouse cardiomyocyte cultures (Figure 4 C), given their relatively mature
168 differentiated state, and compared these to the differentiated H9c2 cells. Using previously
169 published MATLAB scripts (Sun and Südhof, 2021), we analyzed spike amplitude (change
170 in fluorescence from baseline to peak), spike frequency (spikes per minute), and
171 synchronicity (number of spikes occurring at the same time that exceed a threshold based
172 off the mean intensity profile in all the cells in the FOV) (Figure 4 D-I, Table 2). Refer to
173 Table 3 for details of fold change results and statistical analyses. First, to determine
174 whether cell confluence impacts Ca^{2+} handling in differentiated H9c2 cells, we compared
175 two confluences 8.33×10^3 cells/cm^2 (low), as used in the biochemical assays, and 1.0 x

176 10^4 cells/cm^2 (high) at DIV5, the highest confluence before cells started to lift. There were
177 no significant differences between the two confluences in terms of their mean amplitude
178 (Figure 4 D), frequency (Figure 4 E), or synchronous firing rates (Figure 4 F) (Table 3),
179 however, DIV5 high mean frequency was right shifted compared to DIV5 low (Figure 5 H).
180 Ca^{2+} transients of differentiated H9c2 cells were similar in mean amplitude to those of
181 primary cardiomyocytes but exhibited significantly different mean frequency and mean
182 synchronicity. The mean amplitudes observed were 2.36 ± 0.12 for DIV5 low, 2.42 ± 0.21
183 for DIV5 high, 2.36 ± 0.11 for DIV14, and 2.80 ± 0.24 for primary cardiomyocytes (Figure 4
184 D). H9c2 cells displayed significantly different mean frequencies to primary
185 cardiomyocytes with DIV5 low at 3.59 ± 0.25 spikes/min, DIV5 high at 4.03 ± 0.34
186 spikes/min, and DIV14 at 4.37 ± 0.26 spikes/min (Figure 4 E). Similarly, the synchronous
187 firing rate was also significantly different between H9c2 cells and primary cardiomyocytes,
188 with 3.27 ± 0.23 spikes/min for DIV5 low, 4.09 ± 0.47 spikes/min for DIV5 high, and 4.37 ±
189 0.32 spikes/min for DIV14 (Figure 4 F). Primary cardiomyocytes exhibited the highest mean
190 frequency and synchronicity 18.6 ± 3.68 and 18.2 ± 3.53 spikes/min respectively (Table 2).
191 We also analyzed the distributions of these parameters (Figure 4 G-I). Amplitude did not
192 display any noticeable differences between the groups (Figure 4 G). However, the mean
193 frequency and synchronous firing rate for DIV14 cells were both right shifted (Figure 4 H, I),
194 suggesting subpopulations of differentiated cells are approaching Ca^{2+} dynamics that are
195 more similar to those observed in primary cardiomyocytes.
196 Together these results suggest that spontaneous Ca^{2+} transients are comparable
197 between DIV5 and DIV14 differentiated H9c2 cells; yet, while the mean frequency and

198 synchronicity of these transients remain significantly smaller than those of primary
199 cardiomyocytes, subpopulations of differentiated H9c2 cells exhibit shifts towards a more
200 cardiomyocyte-like phenotype with cells displaying increased frequency and synchronous
201 firing rates.
202
203 **H9c2 cell differentiation results in gene expression changes consistent with**
204 **development of a cardiomyocyte phenotype**
205 To begin to understand the mechanisms underlying the observed changes in
206 morphology and Ca^{2+} handling, we probed transcript and protein expression levels of
207 genes involved in transcription, cytoskeleton, ion flux regulation, and signal transduction.
208 We selected genes anticipated to change across cardiomyoblast differentiation based on
209 prior studies (Branco *et al.*, 2015; Kankeu *et al.*, 2018; Campero-Basaldua *et al.*, 2023). We
210 performed RT-qPCR and Western blotting at DIV0, DIV0.5h, DIV3, DIV5, and DIV14 of
211 retinoic acid differentiation. Refer to Table 4 for details of fold change results and
212 statistical analyses. Expression levels of four different genes significantly changed over the
213 time course (Figure 5 A-C). To first confirm retinoic acid signaling pathway activation we
214 measured transcript levels of *Tgm2*, which encodes for transglutaminase 2, and *Rbp2*,
215 which encodes for retinol-binding protein 2 (Balmer and Blomhoff, 2002; Branco *et al.*,
216 2015). As expected, *Tgm2* transcript levels were significantly increased at DIV3 and DIV5
217 (Figure 5 D, E). Within our repertoire of target genes, the earliest transcriptional change
218 was in *Gja5*, which encodes for connexin 40, a gap-junction-forming protein involved in
219 electrical coupling of cardiomyocytes (van Veen *et al.*, 2001) that normally decreases with

220 cardiomyocyte differentiation (Delorme *et al.*, 1995). As anticipated, *Gja5* levels were
221 reduced at DIV0.5, DIV3, and DIV5 (Figure 5 D, F). As expected, the levels of *Cacna1c*,
222 which encodes for the L-type Ca^{2+} channel pore-forming subunit $Ca_v1.2$ crucial in
223 excitation-contraction coupling (Dixon *et al.*, 2012), were also elevated at DIV3 and DIV5
224 (Figure 5 D, G). Transcript levels for *Myom2,* which encodes for myomesin-2, a component
225 of the M-band region in the sarcomere (Lamber *et al.*, 2022), were elevated at DIV5 (Figure
226 5 D, H). Notably the ~18-fold elevation of *Myom2* at DIV5 was the largest increase we
227 observed. We observed no significant differences in any transcript levels between DIV5
228 and DIV14 (Figure 5 J).

229 We further evaluated protein expression changes for a subset of these and
230 additional targets. Refer to Table 4 for details of fold change results and statistical
231 analyses. Notably, levels of vinculin, a protein involved in actin cytoskeleton-membrane
232 linkages and important for cell adhesions (Carisey *et al.*, 2013), were elevated early, at
233 DIV0.5h, and remained increased at DIV3 (Figure 6 A, B). In contrast, levels of Nkx2.5, a key
234 transcription factor and one the earliest markers of cardiac progenitor cells (Cao *et al.*,
235 2023), decreased early at DIV0.5h and continued to decline at DIV3 and DIV5 (Figure 6 A,
236 C). Notably, we detected this band at ~60 kDa, likely the homodimer that Nkx2.5 is known
237 to form when binding DNA (Pradhan *et al.*, 2012). Levels of α-actinin, an F-actin filament
238 cross-linker (Hampton *et al.*, 2007), were reduced at DIV3 (Figure 6 A, D). Vimentin, a type
239 III intermediate filament protein lowly expressed in cardiomyocytes (Kim, 1996), was also
240 decreased at DIV3 and continued to decline at DIV5 (Figure 6 A, E). At DIV3 and DIV5 there
241 was also a slight increase in the levels of GATA4 (Figure 6 A, F), a transcription factor

242 essential for proper cardiac morphogenesis (Grépin *et al.*, 1995; Crispino *et al.*, 2001).
243 Levels of connexin 43, the major gap junction protein in cardiomyocytes (Severs *et al.*,
244 2008), were reduced at DIV3 and DIV5 (Figure 6 A, G). β-actin, was elevated at DIV5 (Figure
245 6 A, H). Levels of cTnT (cardiac troponin T), which is commonly used as a marker of
246 differentiated cardiomyocytes (Forough *et al.*, 2011; Branco *et al.*, 2015), were also
247 significantly increased at DIV5 (Figure 6 A, I). Notably, for β-catenin, which is required early
248 for cardiomyocyte differentiation (Naito *et al.*, 2006; Pahnke *et al.*, 2016), we observed a
249 change in the banding pattern with differentiation. Four of our six replicates showed a
250 distinct 75 kDa lower band at DIV0 and DIV0.5h, which became a less-defined smear
251 between DIV3 and DIV5 (Figure 6 A, L). Representative traces of the β-catenin
252 quantification are shown beside the blot for visualization of the discrete bottom band *vs*
253 smear (Figure 6 A).
254 We next compared gene expression levels of select targets between DIV5 and
255 DIV14 differentiated H9c2 cells and cardiomyocytes. We did this to evaluate which
256 timepoint best approximates the primary cardiomyocyte phenotype at a gene expression
257 level. This allows for comparison to our Ca^{2+} handling data where cardiomyocytes served
258 as our positive control. Refer to Table 4 for details of fold change results and statistical
259 analyses. The only significant transcript difference occurred for *Cacna1c* where expression
260 levels at DIV5 were significantly decreased compared to primary cardiomyocytes;
261 however, this difference was lost by DIV14 (Figure 5 K). When we analyzed the protein
262 levels, we also included embryonic (E15.5) and early postnatal (P2) mouse heart tissue
263 samples as positive controls (Figure 6 M). At DIV5 and DIV14, protein levels of cTnT (Figure

264 6 N) and Nkx2.5 (Figure 6 O) were significantly different from primary cardiomyocytes.
265 Levels of vinculin (Figure 6 Q), α-actinin (Figure 6 R), and vimentin (Figure 6 S) were
266 significantly different from primary cardiomyocytes at DIV5, but not DIV14. In contrast,
267 levels of the 92 kDa β-catenin band were significantly decreased compared to primary
268 cardiomyocytes at DIV14 but not DIV5 (Figure 6T), while the lower molecular weight
269 species of β-catenin showed no difference (Figure 6 U).
270 Together, these data demonstrate that H9c2 cell differentiation alters the
271 expression of several key ion channels and cytoskeleton-associated targets and show that
272 DIV14 cells more closely resemble the primary cardiomyocyte gene expression profile than
273 are DIV5 cells.
274
275 **Discussion**
276 Here we conducted a connected, comprehensive analysis of H9c2 cell morphology,
277 spontaneous Ca^{2+} handling, and gene expression profiles over retinoic acid differentiation.
278 We found that differentiation of H9c2 cells recapitulated nuanced aspects of
279 cardiomyocyte differentiation in all three areas. This model holds relevance for advancing
280 our understanding of the mechanisms underlying inherited heart diseases and potential
281 therapeutic interventions. While further refinements may enhance its accuracy and
282 homogeneity, our results demonstrate that this model reliably captures key features of
283 cardiomyocyte differentiation.
284 Our quantitative analysis of H9c2 cell morphology using high resolution microscopy
285 revealed subpopulation changes in morphologies across H9c2 cell differentiation.

286 Frequency distribution analyses show that subpopulations of cells with increased length,
287 area, perimeter, and nuclei number during differentiation (Figure 2). This may be due to
288 cell-to-cell differences in the levels of retinoic acid receptors, enzymes, and downstream
289 signaling modifications or the extracellular interactions with fibronectin that may limit the
290 differentiation potential. The concentration of fibronectin may be worth while studying
291 further, as a concentration of 2.6 μg/cm^2 has been shown to result in larger cells (Brock
292 and Hörning, 2024), as we used pre-coated coverslips for this, addition of fibronectin may
293 provide a more suitable extracellular matrix for the cells promoting differentiation.
294 Furthermore, on fibroblast-derived matrix, it has been shown that H9c2 cells presented
295 with stronger signals for key markers such as α-actinin and cTnT (Suhaeri *et al.*, 2015). It
296 should be noted that we did not directly compare DIV0 (undifferentiated) with DIV14 and
297 suspect that this comparison would yield significant changes similar to those observed by
298 others (Kankeu *et al.*, 2018; Campero-Basaldua *et al.*, 2023). This highlights the relevance
299 of differentiating H9c2 cells to DIV14 when investigating research questions regarding
300 morphological changes. Other models have also seen specific morphological changes in
301 more differentiated cells compared to undifferentiated ones. For example, in embryonic
302 stem cell-derived cardiomyocytes, the 'late-stage', ~DIV100, cells had increased area,
303 perimeter, percent multinucleation, and eccentricity compared to 'early-stage', ~DIV30
304 cells (Lundy *et al.*, 2013). Another important consideration is culturing protocol as time in
305 culture (Campero-Basaldua *et al.*, 2023) and the addition of molecules such as adhesion
306 factors in 10% FBS (Brock and Hörning, 2024) may significantly impact H9c2 cell
307 differentiation. While 1% FBS with daily supplemental retinoic acid induces differentiation

308 in a subpopulation of cells, further optimization may result in a more homogeneous
309 response.

310 Using super-resolution microscopy, we also observed a notable increase in actin
311 clusters at DIV14 (Figure 3). Actin dynamics are important in regulating cardiomyocyte cell
312 shape and sarcomere formation (Colpan *et al.*, 2021; Grego-Bessa *et al.*, 2023; Fu *et al.*,
313 2024) and while actin clusters are not as characterized in cardiomyocytes, in other cell
314 types these play important roles in regulating actin dynamics, colocalizing with key actin
315 regulators such as actin related protein 2/3 complex and formin (Luo *et al.*, 2016; Xia *et al.*,
316 2019) and even ion channel clustering (Scarselli *et al.*, 2012). In H9c2 cells, future studies
317 could identify if these clusters serve as nucleation points for specific actin-binding
318 proteins or act as scaffolds for signaling complexes using live-cell imaging using
319 fluorescently labeled ion channels or actin regulating proteins and treatments with actin
320 regulating drugs such as latrunculin or jasplakinolide which impair new actin assembly
321 and polymerization.

322 Our analysis of spontaneous Ca^{2+} transients revealed small, non-significant
323 increases in mean Ca^{2+} spike frequency and synchronicity with differentiation, which are
324 statistically different from those in primary cardiomyocytes. Notably, we observed a more
325 pronounced shift in these parameters between DIV5 low and DIV14 H9c2 cells, which were
326 seeded at a more comparable density, suggesting that differentiation may lead to subtle
327 changes in Ca^{2+} handling that could have functional implications (Figure 4). Although these
328 levels never reached those of primary cardiomyocytes, DIV14 Ca^{2+} frequency and
329 synchronous firing rates were right shifted, indicating an increased number of cells

330 exhibiting coordinated activity akin to that seen in primary cardiomyocytes. These changes
331 are consistent with prior work where H9c2 cell differentiation increased the expression of
332 genes regulating Ca^{2+} homeostasis, including cardiac-specific L-type Ca^{2+} channel
333 isoforms, *Serca2*, and *RyR2* (Branco *et al.*, 2015; Campero-Basaldua *et al.*, 2023). In our
334 study we saw an increase in *Cacna1c* levels at DIV3 and DIV5 (Figure 5) which may have
335 contributed to the presence of Ca^{2+} dynamics seen in DIV5 and DIV14 cells. In response to
336 caffeine, increased Ca^{2+} transient amplitudes and increased responding cell density were
337 observed at DIV7 suggesting increased RyR function and/or expression (Campero-
338 Basaldua *et al.*, 2023). Given that there are alternations in Ca^{2+} dynamics when induced by
339 caffeine, future studies may explore the molecular foundations responsible for the
340 spontaneous Ca^{2+} transients observed in differentiated H9c2 cells.
341 Along with the increased expression of Ca^{2+} homeostasis-related genes,
342 differentiated H9c2 cells upregulate transcript and protein expression levels of key
343 cardiomyocyte markers (Branco *et al.*, 2015; Kankeu *et al.*, 2018; Campero-Basaldua *et al.*,
344 2023). To provide a potential mechanism underlying the observed morphological and
345 functional changes, increases in multiple cytoskeletal genes and proteins and an ion
346 channel gene were observed which may contribute to the increased length, perimeter, and
347 area as well as the Ca^{2+} handling in these cells (Figures 5,6). Our findings are in line with
348 the literature as we saw significant increases in both transcript and protein expression of
349 *Tnnt2* and increased expression of *Cacna1c* ($Ca_v1.2$) (Branco *et al.*, 2015; Kankeu *et al.*,
350 2018; Campero-Basaldua *et al.*, 2023), a decrease in *Pde4a* transcript levels (Branco *et al.*,
351 2015), and no changes to *Gata4* transcript expression levels (Branco *et al.*, 2015). We

352 observed our greatest increase in *Myom2* which has also been reported (Branco *et al.*,
353 2015). This in combination with the decrease in vimentin, an intermediate filament protein
354 that is weakly expressed in cardiomyocytes, suggests that differentiated H9c2 cells
355 undergo morphological gene expression changes resembling those of cardiomyocytes.
356 This shift further indicates that key signaling pathways and cytoskeletal remodeling
357 processes involved in cardiomyocyte maturation may be preserved in H9c2 cells. Another
358 interesting finding included the band patterning of β-catenin. At DIV0, 4 of 6 replicates
359 showed a distinct 75 kDa band, which by DIV5, was replaced by a higher molecular weight
360 smear. During liver development, the truncated 75 kDa isoform resulting from calpain
361 cleavage, promotes hepatocyte differentiation; however, retaining the full-length isoform
362 promotes biliary epithelial cell differentiation (Lade *et al.*, 2012). A similar mechanism may
363 exist in cardiomyocytes, where β-catenin is developmentally downregulated during
364 cardiomyocyte differentiation, coinciding with loss of proliferation in mature
365 cardiomyocytes (Quaife-Ryan *et al.*, 2020). It could be that specific transcriptionally active
366 isoforms may contribute to different roles of β-catenin depending on the maturation state
367 of cardiomyocytes, similar to what has been shown in the liver.
368 We also assessed gene and protein expression in H9c2 cells at DIV5 and DIV14 to
369 determine which timepoint more closely resembles primary cardiomyocytes. While
370 nuanced with some proteins showed significant differences at both timepoints and many
371 transcript levels were not significantly different. Our analysis suggests that DIV14 cells
372 generally align more closely with primary cardiomyocytes than DIV5 with *Cacna1c*
373 transcript levels as well as vinculin, α-actinin, and vimentin protein levels not being

374 significantly different from those observed in primary cardiomyocytes while they were
375 significantly different between DIV5 and primary cardiomyocytes. These results indicate
376 that differentiating H9c2 cells to DIV14 may be more appropriate, especially when
377 research questions involve key cardiomyocyte ion channel and cytoskeletal proteins.
378 Additionally, H9c2 cells are easy to transfect (Figure 7 A) and the use of inducible vectors
379 allows for the study of different variants at various stages of differentiation (Figure 7 B).
380 Compared to primary cardiomyocytes, which are more difficult to isolate and maintain,
381 H9c2 cells offer a more robust and high-throughput model. Given we saw morphological,
382 functional, and gene expression changes that occur during H9c2 cell differentiation,
383 studies investigating the impact of variants on the degree of these changes can be studied.
384

385 **Translational implications**

386 The ability of differentiated H9c2 cells to model key morphological, functional, and gene
387 expression features of cardiomyocytes highlights their relevance as a model system for
388 investigating the cellular and molecular mechanisms underlying cardiac development and
389 disease. While this differentiation is nuanced and subpopulations of cells were more
390 differentiated than others, the ability to model cardiomyocyte differentiation in a robust
391 and easily manipulated cell line allows for experiments including prioritizing hypotheses
392 before advancing to more complex models and high throughput screenings of
393 therapeutics. Furthermore, the ease of transfection and use of inducible vectors enables
394 the investigation of the impacts of genetic variants at various stages of cardiomyocyte
395 differentiation. Overall, the morphological, functional, and gene expression changes that

396 occur across differentiation indicate that H9c2 cells are useful for identifying disease
397 mechanisms, therapeutic targets, and developing interventions.
398
399 **Limitations**
400 One of the challenges in measuring the morphology of H9c2 cells is the proximity of
401 cells; however, this feature itself is a critical process during cardiomyocyte development
402 and in diseased states (McCain and Parker, 2011; Kowalski *et al.*, 2017). As a result, the
403 segmentation was challenging given the strong expression of actin stress fibers throughout
404 the cell. To measure the morphology of H9c2 cells we identified the number of
405 segmentable cells (cells with clear boundaries) in an FOV and randomly selected 3 cells.
406 Inherently, this may have favoured the more undifferentiated cells in the FOV as they are
407 less aligned by nature. Future studies could employ cell perimeter stains such as wheat
408 germ agglutinin for easier analysis and to better quantify the whole region of interest. For
409 the morphological analysis we had 2 separate groups of analysis (DIV0 and DIV5 and then
410 DIV5 and DIV14). The latter group was seeded at a lower density to prevent cells from
411 becoming too confluent and lifting and as a result this may have altered the morphology as
412 seen by differences in the maximum values for length and perimeter. It is also likely that
413 there would be more significant differences in the measured values if we compared DIV0
414 to DIV14 than from DIV0 to DIV5 and so another analysis comparing DIV0, DIV5, and DIV14
415 may provide useful measures of how cell shape changes over differentiation.
416 Due to logistical limitations, we performed the Ca^{2+} imaging for different
417 experimental groups on different days. DIV5s were imaged on the same day; however,

418 DIV14 and primary cardiomyocytes were imaged on separate days. In future work, we
419 suggest that a final stimulated Ca^{2+} spike could be used to normalize amplitudes, for
420 example.

421 In the present study, for the primary cardiomyocytes, we performed mixed sex
422 cultures. Given the known sex differences in heart disease, the development of single
423 heart cultures may explain some differences between H9c2 cells and the models as H9c2
424 cells were isolated from a female left ventricle. Furthermore, the quantification of primary
425 cardiomyocyte culture composition may also explain differences if some cultures contain
426 more endothelial or fibroblast cells. And given the benefit of having a culture more
427 resembling what is seen *in vivo* it may be worthwhile to maintain the presence of
428 endothelial cells and fibroblasts. Finally, in future work, the sex of the animal from which
429 all heart tissues are derived should be recorded.

430

431 **Conclusions**

432 The H9c2 rat ventricular cardiomyoblast cell line has been used to model cardiomyocyte
433 development and disease. Here we quantified changes in three broad areas of H9c2 cell
434 biology across five and fourteen days of retinoic acid differentiation: morphology,
435 Ca^{2+}handling, and gene expression. Depending on the context, we compared to
436 undifferentiated cells or primary cardiomyocytes. Overall, we saw differentiation-induced
437 changes in subpopulations of cells in all three areas. These characteristics position H9c2
438 cells as a high-throughput model for studying genetic and environmental factors affecting
439 cardiomyocyte biology, with the advantage of easier and shorter culturing protocols.

440 Additionally, their ease of transfection allows for targeted investigation of specific genes
441 and pathways, and the impacts of variants on cardiomyocyte differentiation. Our
442 comprehensive characterization indicates that H9c2 cells are a useful model in
443 investigating components of cardiomyocyte differentiation and may be particularly useful
444 for understanding disease mechanisms and for screening potential therapeutic
445 interventions. However, the heterogenicity of differentiated H9c2 cell analysis should take
446 into account the spread of differentiated cells and the addition of other models such as
447 primary cardiomyocytes and iPSC-derived cardiomyocytes may be of value to validate the
448 findings.
449

450 **Materials and Methods**

451 **Cell culture**

452 The H9c2 rat ventricular-derived cardiomyoblast cell line was obtained from the
453 American Type Culture Collection (ATCC, CRL-1446). H9c2 cells were cultured in
454 Dulbecco's Modified Eagle Medium (DMEM, ATCC, 30-2002) supplemented with 10% fetal
455 bovine serum (FBS) (Thermo Fisher, 12483020, reserve 10498874), 100 U/mL penicillin,
456 and 100 µg/mL streptomycin (Thermo Fisher, 15140122) at 37°C in 5% CO_2. Cells were
457 kept at or below 15 passages and passaged at 70-80% confluence to prevent the loss of
458 differential potential. Each vial was tested for mycoplasma contamination using the
459 universal mycoplasma detection kit (ATCC, 30-1012K).

460 H9c2 cells were differentiated as previously described (Ménard *et al.*, 1999). Briefly,
461 cells to be collected within 5 days were seeded at 8,333 cells/cm^2 for Western blotting and

462 RNA experiments, 8,000 cells/cm^2 for immunocytochemistry experiments, and either
463 8,333 cells/cm^2 or 10,000 cells/cm^2 for live cell Ca^{2+} imaging experiments. For cells
464 collected at 14 days, cell densities were decreased by half to prevent cells from becoming
465 confluent and detaching. One day after seeding, FBS was decreased from 10% to 1% and
466 media was supplemented with 1 μM all-trans retinoic acid (ATRA) (Sigma, R2625-50MG).
467 ATRA was added daily, in the dark, and cells were collected prior to ATRA treatment (DIV0),
468 at 5 hours (DIV0.5), 3 days (DIV3), 5 days (DIV5), and 14 days (DIV14) post ATRA treatment.
469 Sample size was chosen based from the resource equation (Arifin and Zahiruddin, 2017).
470 One day after seeding, cells were transfected with a tetracycline inducible pCMB6-
471 AC-GFP-rtTA plasmid (Origene, PS100125) using jetPEI (Figure 7). 4 μL of jetPEI diluted in
472 150 mM NaCl was added to 2 μg of plasmid DNA also diluted in 150 mM NaCl, the mixture
473 was incubated for 15 minutes, and then added dropwise to the cells in DMEM containing
474 no antibiotics. One day after transfection, media was changed to DMEM containing 1%
475 FBS, 100 U/mL penicillin, and 100 μg/mL streptomycin, and was treated daily with 1 μM
476 ATRA. To induce GFP expression, 10 ng/mL Doxycycline hyclate (Sigma, D9891-1G) was
477 added to the differentiation media.
478
479 **Experimental Animals**
480 All animal procedures were approved by the University of Victoria Animal Care
481 Committee and performed in accordance with the guidelines set by the Canadian Council
482 on Animal Care. Male and female embryonic day (E)15.5– postnatal day (P)2 mice were
483 used in this study. C57BL/6J mice were obtained from The Jackson Laboratory (#000664).

484 Mice were housed under a 12/12 hour light/dark cycle starting at 8 A.M., with food and
485 water ad libitum; temperature was maintained between 20°C and 25°C and humidity at 40–
486 65%. Sample size was chosen based from the resource equation (Arifin and Zahiruddin,
487 2017).
488
489 **Heart Tissue Extraction**
490 E15.5 and P2 heart tissue was flash frozen in liquid nitrogen and stored at -80°C.
491 E15.5 heart tissue intended for RNA analysis was stored in RNAlater Stabilization Solution
492 (Thermo Fisher, AM7020). Heart tissue was homogenized in a Dounce homogenizer on ice
493 with either 100 µL TRIzol (Thermo Fisher, 15596026) per 5-10 mg tissue (RNA) or RIPA lysis
494 buffer (9.1 mM PBS, 150 mM NaCl, 1.7 mM monobasic sodium phosphate, 9.1 mmol/L
495 dibasic sodium phosphate, 1% Igepal, 0.5% w/v sodium deoxycholate, 0.1% sodium
496 dodecyl sulphate (SDS), 10 µL/mL protease inhibitor cocktail (Sigma, P8340-5ML))
497 (protein). RNA was extracted from tissue samples after incubating on ice for 5 minutes and
498 then stored in TRIzol at -80°C. Protein lysates were pushed through a 27 ½ gauge needle 2
499 times and incubated on ice for 30 minutes; samples were then centrifuged at 13500 x g for
500 20 minutes at 4°C and the supernatant was also frozen at -80°C.
501
502 **Primary culture isolation**
503 Mouse cardiomyocytes were isolated according to standard methods previously
504 described (Ehler *et al.*, 2013). 6-10 hearts were used per each given culture, representing 1
505 biological replicate (N). Briefly, hearts were extracted from P1-P2 mice and transferred into

506 phosphate-buffered saline solution (without Ca^{2+} or Mg^{2+}) containing 20 mM 2,3-
507 Butanedione monoxime (BDM) (Sigma, B0753). In a sterile cell culture hood, the hearts
508 were washed, minced, and submerged in isolation medium consisting of Hanks' Balanced
509 Salt Solution (HBSS) with 20 mM BDM and 0.025% Trypsin (Gibco, 15090-046) for
510 incubation overnight under gentle agitation at 4°C. After incubation, the isolation medium
511 was removed, and the tissue was oxygenated in Leibovitz's L-15 medium containing 10 mM
512 BDM and 0.75 mg/ml of Collagenase/Dispase® mixture (Roche, 10269638001), then placed
513 in a shaking incubator for 30 minutes at 37°C. To release cells into suspension, the tissue
514 fragments were gently triturated and filtered through a 100 µm nylon mesh cell strainer.
515 Cells were centrifugated at 200 x g for 5 minutes to remove fibroblasts and endothelial
516 cells. The resulting pellet was resuspended in Dulbecco's modified Eagle's medium
517 (DMEM) supplemented with 5% Heat Inactivated Horse Serum (Thermo Fisher, 26050070)
518 and plated in a cell culture dish (a pre-plating step that removes many of the remaining
519 fibroblasts and endothelial cells). After a 2-3 hour incubation, non-adherent
520 cardiomyocytes were collected and plated on pre-coated collagen coverslips (Neuvitro,
521 NEU-GG-12-1.5-COLLAGEN) or onto collagen from calf skin (Fisher, ICN16008410) coated
522 35 mm glass bottom imaging dishes at a density of 1.5×10^5 cells per cm^2. The following
523 day, plating medium was replaced by DMEM containing 5% HIHS, 100 U/mL penicillin, and
524 100 µg/mL streptomycin for maintenance.
525
526 **Immunocytochemistry**

527 H9c2 cells were seeded onto fibronectin coated coverslips either purchased from
528 Neuvitro (NEU-GG-12-1.5-FIBRONECTIN) or coated in lab using fibronectin bovine plasma
529 (Sigma, F1141-1MG). Coverslips were fixed with 4% paraformaldehyde for 5 minutes at
530 DIV0, DIV5, and DIV14, followed by three washes with PBS containing Ca^{2+} or Mg^{2+}. Cells
531 were permeabilized with 0.1% Tween-20 for 5 minutes, washed three times in PBS as
532 before, blocked with 1% BSA and 22.52 mg/mL glycine in PBS-T, and then were incubated
533 in primary antibody (1:500 Proteintech TOM20 (Thermo Fisher, 11802-1-AP)) diluted in 1%
534 BSA in PBS-T overnight at 4°C in a humidified chamber. After primary antibody incubation,
535 coverslips were washed three times in PBS and then incubated with 1:800 Alexa Fluor 488
536 (Jackson Immuno Research, 711-545-152), Hoechst (1:500), and phalloidin (1:500; 555,
537 Invitrogen, A34055; Acti-Stain 670, Cytoskeleton, PHDN1) diluted in 1% BSA in PBS
538 overnight at room temperature for 1 hour. Following secondary incubation, coverslips were
539 washed three additional times, and mounted with ProLong Gold Antifade Mountant
540 (Thermo Fisher, P10144).
541 For transfected cells, fixation with 4% paraformaldehyde was performed as
542 previously described, followed by three washes in dPBS and mounting with ProLong Gold
543 Antifade Mountant.
544
545 **Microscopy**
546 Cells were imaged using a Leica TCS SP8 confocal microscope with HyD detectors. For
547 DIV0 versus DIV5 comparisons, imaging was performed using a 40X oil-immersion
548 objective set at 0.75 zoom (1.30 NA, pinhole = 65.28 µm, 3904 x 3904 (pixel size = 74.46 x

549 74.46 nm)). For DIV5 versus DIV14 cells, images were acquired using the 20X dry-objective
550 (0.7 NA, pinhole = 60.69 µm, 3800 x 3800 (pixel size =148.92 nm x 148.92 nm)).
551 For transfected cells, images were acquired using the 40X oil-immersion objective
552 set at 0.75 zoom (1.30 NA, pinhole = 65.08 µm, 2048 x 2048 (pixel size = 141.98 nm x
553 141.98 nm)). GFP was excited using the 488 nm Argon laser at 10% intensity.
554 STED images were acquired using a 100X oil-immersion objective (1.40 NA, pinhole
555 = 117.5 µm, pixel size optimized to 20 µm x 20 µm) at a zoom of 2. Phalloidin 555 was
556 excited using the 514 Argon laser at 20% intensity. Fluorescence was captured using the
557 HyD detector using the 660 STED laser at 25% 3D, 80% intensity and 70-90% power.
558 For all images presented, brightness and contrast were uniformly adjusted for
559 presentation purposes.
560
561 **Morphology Analysis**
562 To analyze morphological features of H9c2 cells, a custom Matlab script was
563 created: Morphology Analysis Overview A (code available at
564 https://github.com/SwayneLab/Quantification-of-H9c2-cell-differentiation-/). Images
565 were blinded before analysis. First, the analysis region for each cell was marked by
566 manually drawing a polygon around it. The script processed a binarized image where cell
567 pixels are set to one and background pixels to zero. Zeros were padded around the image
568 to ensure accurate boundary detection at the edges. The cell boundary was identified by
569 examining each pixel and its eight surrounding neighbours in a three x three grid, with
570 boundary pixels identified whenever a surrounding pixel was zero. Next, a covariance

571 matrix was created from these repositioned coordinates. An eigenvalue decomposition
572 was performed on this matrix to find the principal directions in which the cell extended.
573 These principal directions correspond to the longest (major) and shortest (minor)
574 dimensions of an ellipse that could fit around the cell.

575 Length, area, and eccentricity were calculated by first finding the center point, or
576 centroid, of each cell, averaging the positions of all the pixels that made up the cell. This
577 average point helped reposition the cell's pixel distribution to the center of the coordinate
578 system for easier analysis. Length was calculated from the square root of the largest
579 eigenvalue (major axis) and eccentricity was calculated from the ratio of largest eigenvalue
580 (major axis) to smallest eigenvalue (minor axis). The perimeter was calculated by counting
581 the number of boundary pixels, and area was calculated from filling in pixel area between
582 the boundary pixels. The number of nuclei per analyzed cell was calculated manually. All
583 plots and statistics were performed in R (Superplot code edited from (Lord *et al.*, 2020)),
584 frequency distributions were created in Prism 10 for Mac OS X (version 10.3.1, GraphPad
585 Software, Inc.).

586

587 **Calcium imaging and analysis**

588 Isolated mouse cardiomyocytes seeded in collagen-coated 35 mm glass bottom imaging
589 dishes (ibidi, 81218-200) were loaded with cell-permeant 4 μM Fluo-4 AM (Invitrogen, F-
590 14201) for 35 minutes. H9c2 cells seeded in fibronectin-coated imaging dishes (ibidi,
591 81218-200) were loaded with 1.5 μM Fluo-4 AM at room temperature for 25 minutes.
592 Incubation time, temperature, and loading concentrations were optimized for each cell

593 type to prevent dye toxicity and compartmentalization. The cells were subsequently
594 washed using HBSS with 10 mM HEPES (Stem Cell Technologies, 37150) and incubated for
595 20 minutes to allow for de-esterification of the AM esters. All samples were imaged in
596 complete FluoroBrite™ DMEM media (Gibco™, A1896701) at 37°C and 5% CO_2 in a Tokai Hit
597 Stage Top Incubation System mounted on the Leica SP8. Fluo-4 was excited with the 488
598 nm argon laser line at 20% intensity through a 20x objective (0.70 NA, pinhole =242.65 µm).
599 Using the Leica SP8 resonant scanner, cardiomyocytes were imaged at 27.7 FPS for 1
600 minute and H9c2 cells were imaged at 14.6 FPS for 2 minutes. A minimum of 2 dishes were
601 imaged per biological replicate with 2-5 fields of view captured per dish.
602 Imaging files were initially processed by EZcalcium, an open-source, automated data
603 analysis package (Cantu *et al.*, 2020). Part of the Matlab-based toolbox, the automated
604 ROI detection module was run first to detect all active cells, followed by the ROI
605 refinement module to semi-automatically eliminate dying cells and those with a poor
606 signal/noise. Minor movement artefacts in some FOV were not deemed significant by the
607 motion correction module. For quantification of the extracted data files, a series of Matlab
608 scripts based on those published (Sun and Südhof, 2021) were employed. All data were
609 analyzed and plotted in R, frequency distributions were created in Prism 10 for Mac OS X
610 (version 10.3.1, GraphPad Software, Inc.).
611
612 **RNA extraction**

613 RNA was isolated using TRIzol as in (Chomczynski, 1993). Briefly, RNA from H9c2
614 cells or primary cardiomyocytes was collected by adding 0.4 mL TRIzol per $1x10^5$-$1x10^7$
615 cells. Extracted RNA was stored at -80°C.
616 RNA integrity was checked using the Agilent RNA 6000 Nano Kit (Agilent, 5067-
617 1511). Briefly, to minimize secondary structure, 2 µL RNA was denatured at 70°C for 2 min.
618 1 µL was loaded into the primed chip containing the gel-dye mix and RNA 6000 nano
619 marker. Once loaded, the chip was vortexed at 2400 rpm for 60 sec in the IKA vortex mixer,
620 loaded into the Agilent 2100 bioanalyzer, and the total RNA (eukaryotic) run was started
621 within 5 minutes. The RNA integrity number (RIN) scores were above 8.8 for H9c2 samples,
622 7.6 for P2 heart tissue and primary cardiomyocytes, and 1.5 for the E15.5 sample which
623 showed both the 18S and 28S bands.
624
625 **RT-qPCR**
626 1000 ng of RNA underwent treatment with DNase1 (Thermo Fisher, EN0521) to
627 digest any potential double-stranded DNA isolated with the RNA. cDNA was synthesized
628 from 500 ng of the DNase1 treated RNA using the Maxima First Strand cDNA Synthesis Kit
629 using random primers (Thermo Fisher, K1652). For each RT+ reaction, an RT- reaction was
630 also run. A GAPDH PCR reaction was run to confirm the cDNA synthesis and validate the
631 RT- controls on a 2% agarose gel. qPCR reactions for genes of interest were performed on a
632 QIAquant 96 well 5 plex qPCR machine (Qiagen, 9003010). Using PrimeTime qPCR probe
633 assays (IDT) and PrimeTime gene expression master mix (IDT, 1055772), 100 µg of RNA was
634 run in 10 µL reactions. The probe assays used are listed in Table 6. Standard cycling

635 conditions were run: polymerase activation at 95°C for 3 minutes, followed by 45 cycles of
636 denaturation at 95°C for 15 seconds and annealing/extension at 60°C for 1 minute. RT-
637 qPCR data was inputted into geNorm to determine the best normalization strategy
638 (Vandesompele *et al.*, 2002). To normalize target genes, relative expression was calculated
639 using the geometric mean of two housekeeping genes, *Polr2a* and *Ppia*. To generate the
640 heat maps, genes were calculated as percent control and presented as log2 fold change
641 using pheatmap in R (Figure 5, Table 4). Graphs were created in Prism 10 for Mac OS X
642 (version 10.3.1, GraphPad Software, Inc.).
643
644 **Western Blotting**
645 Adhered cells were washed 2 times in dPBS and lysed in RIPA lysis buffer (9.1 mM
646 PBS, 150 mM NaCl, 1.7 mM monobasic sodium phosphate, 9.1 mmol/L dibasic sodium
647 phosphate, 1% Igepal, 0.5% w/v sodium deoxycholate, 0.1% sodium dodecyl sulphate
648 (SDS), 10 µL/mL protease inhibitor cocktail (Sigma, P8340-5ML)) by scraping cells off the
649 plate or coverslip on ice. Cell lysates were then treated as described for the mouse heart
650 tissue. Protein content was determined using the DC protein assay (Bio-rad, 5000112). 10
651 µg of protein was incubated in Laemmli sample buffer (1X: 0.08 mM bromophenol blue,
652 0.05 M Tris-HCl pH 6.8, 0.058 M SDS, 3.33% v/v glycerol) at room temperature under
653 reducing conditions (5% dithiothreitol (DTT) and 5% β-mercaptoethanol), separated by
654 SDS-PAGE on TGX-stain free gels (Bio-rad, 4561094) and transferred to either a 0.2 µm
655 pore PVDF membrane (Bio-rad, 1620177) for peroxidase detection using the Syngene
656 G:Box imager or a 0.45 µm pore LF-PVDF membrane (Sigma, IPFL00010) for fluorescent

657 detection using the Licor Odyssey CLx Imager. For Western blots using the peroxidase-
658 based detection, the membrane was blocked with 5% fat free instant skim milk in TBS-T,
659 then incubated with indicated antibodies in the blocking solution, and protein bands were
660 visualized using the Clarity Western enhanced chemiluminescence substrate (Bio-Rad,
661 1705061). For Western blots using the fluorescent-based detection, the membrane was
662 blocked with intercept (TBS) blocking buffer (Li-cor, 927-60003), incubated with indicated
663 antibodies in the blocking solution containing 0.1% Tween 20 and 0.01% SDS (secondary
664 only). All proteins were normalized to total protein using Ponceau S Solution (0.1% w/v in
665 5% acetic acid) (Sigma, P7170-1L) or the Revert 700 Total Protein Stain (Li-cor, 926-11010)
666 and quantified with ImageJ. The antibodies and concentrations used are listed in Table 7.
667 Graphs were created in Prism 10 for Mac OS X (version 10.3.1, GraphPad Software, Inc.).
668

669 **Acknowledgements**

670 This work was supported by a Canadian Institutes for Health Research Project Grant
671 (CIHR; PJT-169064) awarded to LTA and LAS. NY was supported by a Vanier Canada
672 Graduate Scholarship (Canadian Institutes of Health Research Vanier) and University of
673 Victoria Donor Awards. We acknowledge that this research was conducted on the
674 traditional territory of the Lək̓ʷəŋən (Songhees and Esquimalt) Peoples, and the Lək̓ʷəŋən
675 and W̱SÁNEĆ Peoples whose historical relationships with the land continue to this day. We
676 also acknowledge the Gitxsan peoples and their leadership as this work was initiated for
677 and is foundational for our ongoing research partnership on the mechanisms of inherited

678 cardiac disease. The progress of this work has been presented at in-person community
679 gatherings, and virtually by NY.
680

681 **Author contributions**

682 NY, JR, LA, and LAS conceived and designed the experiments. NY conducted the cell
683 culture work, morphological imaging, and biochemical assays, as well as advised in the
684 morphological and Ca^{2+} analyses. MRM created the morphological analysis, which both
685 MRM and RS conducted, NY then graphed and analyzed. JR and NY isolated primary
686 cardiomyocyte cultures. JR performed all Ca^{2+} imaging and analysis, as well as directed the
687 creation and statistical analysis for Figure 4. NY conducted all statistical analysis, RS
688 created the superplot code in R. NY and KWLF created all figures and supplemental
689 videos. NY, JR, RS, KWLF, LEWS, LA, and LAS wrote and edited the manuscript.
690

691 **References**

692 Ahuja, P, Sdek, P, and Maclellan, WR (2007). Cardiac Myocyte Cell Cycle Control in
693 Development, Disease and Regeneration. Physiol Rev 87, 521–544.

694 Arifin, WN, and Zahiruddin, WM (2017). Sample Size Calculation in Animal Studies Using
695 Resource Equation Approach. Malays J Med Sci 24, 101–105.

696 Avanzato, D, Merlino, A, Porrera, S, Wang, R, Munaron, LM, and Mancardi, D (2014). Role of
697 calcium channels in the protective effect of hydrogen sulfide in rat cardiomyoblasts. Cell Physiol
698 Biochem 33, 1205–1214.

699 Balmer, JE, and Blomhoff, R (2002). Gene expression regulation by retinoic acid. Journal of
700 Lipid Research 43, 1773–1808.

701 Branco, AF, Pereira, SP, Gonzalez, S, Gusev, O, Rizvanov, AA, and Oliveira, PJ (2015). Gene
702 expression profiling of H9c2 myoblast differentiation towards a cardiac-like phenotype. PLoS
703 ONE 10, e0129303.

704 Brock, J, and Hörning, M (2024). Optimization of H9c2 differentiation leads to calcium-active
705 and striated cardiac cells without addition of retinoic acid. 2024.09.24.614681.

706 Campero-Basaldua, C, Herrera-Gamboa, J, Bernal-Ramírez, J, Lopez-Moran, S, Luévano-
707 Martínez, L-A, Alves-Figueiredo, H, Guerrero, G, García-Rivas, G, and Treviño, V (2023). The
708 retinoic acid response is a minor component of the cardiac phenotype in H9c2 myoblast
709 differentiation. BMC Genomics 24, 431.

710 Cantu, DA, Wang, B, Gongwer, MW, He, CX, Goel, A, Suresh, A, Kourdougli, N, Arroyo, ED,
711 Zeiger, W, and Portera-Cailliau, C (2020). EZcalcium: Open-Source Toolbox for Analysis of
712 Calcium Imaging Data. Front Neural Circuits 14, 25.

713 Cao, C, Li, L, Zhang, Q, Li, H, Wang, Z, Wang, A, and Liu, J (2023). Nkx2.5: a crucial regulator
714 of cardiac development, regeneration and diseases. Front Cardiovasc Med 10, 1270951.

715 Carisey, A, Tsang, R, Greiner, AM, Nijenhuis, N, Heath, N, Nazgiewicz, A, Kemkemer, R,
716 Derby, B, Spatz, J, and Ballestrem, C (2013). Vinculin Regulates the Recruitment and Release of
717 Core Focal Adhesion Proteins in a Force-Dependent Manner. Curr Biol 23, 271–281.

718 Carton, F, Casarella, S, Di Francesco, D, Zanella, E, D'urso, A, Di Nunno, L, Fusaro, L, Cotella,
719 D, Prat, M, Follenzi, A, *et al.* (2023). Cardiac Differentiation Promotes Focal Adhesions
720 Assembly through Vinculin Recruitment. Int J Mol Sci 24, 2444.

721 Chomczynski, P (1993). A reagent for the single-step simultaneous isolation of RNA, DNA and
722 proteins from cell and tissue samples. Biotechniques 15, 532–534, 536–537.

723 Colpan, M, Iwanski, J, and Gregorio, CC (2021). CAP2 is a regulator of actin pointed end
724 dynamics and myofibrillogenesis in cardiac muscle. Commun Biol 4, 365.

725 Crispino, JD, Lodish, MB, Thurberg, BL, Litovsky, SH, Collins, T, Molkentin, JD, and Orkin,
726 SH (2001). Proper coronary vascular development and heart morphogenesis depend on
727 interaction of GATA-4 with FOG cofactors. Genes Dev 15, 839–844.

728 Delorme, B, Dahl, E, Jarry-guichard, T, Marics, I, Briand, J-P, Willecke, K, Gros, D, and
729 Théveniau-Ruissy, M (1995). Developmental regulation of connexin 40 gene expression in
730 mouse heart correlates with the differentiation of the conduction system. Developmental
731 Dynamics 204, 358–371.

732 Dixon, RE, Yuan, C, Cheng, EP, Navedo, MF, and Santana, LF (2012). Ca2+ signaling
733 amplification by oligomerization of L-type Cav1.2 channels. Proc Natl Acad Sci U S A 109,
734 1749–1754.

735 Ehler, E, Moore-Morris, T, and Lange, S (2013). Isolation and Culture of Neonatal Mouse
736 Cardiomyocytes. J Vis Exp, e50154.

737 Forough, R, Scarcello, C, and Perkins, M (2011). Cardiac Biomarkers: a Focus on Cardiac
738 Regeneration. J Teh Univ Heart Ctr 6, 179–186.

739 Fritzsche, M, Li, D, Colin-York, H, Chang, VT, Moeendarbary, E, Felce, JH, Sezgin, E, Charras,
740 G, Betzig, E, and Eggeling, C (2017). Self-organizing actin patterns shape membrane
741 architecture but not cell mechanics. Nat Commun 8, 14347.

742 Fu, W, Liao, Q, Shi, Y, Liu, W, Ren, H, Xu, C, and Zeng, C (2024). Transient induction of actin
743 cytoskeletal remodeling associated with dedifferentiation, proliferation, and redifferentiation
744 stimulates cardiac regeneration. Acta Pharm Sin B 14, 2537–2553.

745 Gee, KR, Brown, KA, Chen, W-NU, Bishop-Stewart, J, Gray, D, and Johnson, I (2000).
746 Chemical and physiological characterization of fluo-4 Ca2+-indicator dyes. Cell Calcium 27,
747 97–106.

748 Grego-Bessa, J, Gómez-Apiñaniz, P, Prados, B, Gómez, MJ, MacGrogan, D, and de la Pompa,
749 JL (2023). Nrg1 Regulates Cardiomyocyte Migration and Cell Cycle in Ventricular
750 Development. Circ Res 133, 927–943.

751 Grépin, C, Robitaille, L, Antakly, T, and Nemer, M (1995). Inhibition of transcription factor
752 GATA-4 expression blocks in vitro cardiac muscle differentiation. Mol Cell Biol 15, 4095–4102.

753 Hampton, CM, Taylor, DW, and Taylor, KA (2007). Novel structures for α-actinin: F-actin
754 interactions and their implications for actin-membrane attachment and tension sensing in the
755 cytoskeleton. J Mol Biol 368, 92–104.

756 Harvey, RD, and Hell, JW (2013). CaV1.2 Signaling Complexes in the Heart. J Mol Cell Cardiol
757 58, 143–152.

758 Hescheler, J, Meyer, R, Plant, S, Krautwurst, D, Rosenthal, W, and Schultz, G (1991).
759 Morphological, biochemical, and electrophysiological characterization of a clonal cell (H9c2)
760 line from rat heart. Circulation Research 69, 1476–1486.

761 Hirschy, A, Schatzmann, F, Ehler, E, and Perriard, J-C (2006). Establishment of cardiac
762 cytoarchitecture in the developing mouse heart. Developmental Biology 289, 430–441.

763 Inácio, JM, Nunes, MM, Almeida, M, Cristo, F, Anjos, R, and Belo, JA (2023). Gene-Edited
764 Human-Induced Pluripotent Stem Cell Lines to Elucidate DAND5 Function throughout Cardiac
765 Differentiation. Cells 12, 520.

766 Kankeu, C, Clarke, K, Van Haver, D, Kris Gevaert, bcd, Francis Impens, bc, Anna Dittrich,
767 bcd, Llewelyn Roderick, H, Passante, E, and Huber, HJ (2018). Quantitative proteomics and
768 systems analysis of cultured H9C2 cardiomyoblasts during differentiation over time supports a
769 "function follows form" model of differentiation. 14, 181.

770 Kim, H-D (1996). Expression of intermediate filament desmin and vimentin in the human fetal
771 heart. The Anatomical Record 246, 271–278.

772 Kimes, BW, and Brandt, BL (1976). Properties of a clonal muscle cell line from rat heart.
773 Experimental Cell Research 98, 367–381.

774 Kowalski, WJ, Yuan, F, Nakane, T, Masumoto, H, Dwenger, M, Ye, F, Tinney, JP, and Keller,
775 BB (2017). Quantification of Cardiomyocyte Alignment from Three-Dimensional (3D) Confocal
776 Microscopy of Engineered Tissue. Microscopy and Microanalysis 23, 826–842.

777 Lade, A, Ranganathan, S, Luo, J, and Monga, SPS (2012). Calpain Induces N-terminal
778 Truncation of β-Catenin in Normal Murine Liver Development. J Biol Chem 287, 22789–22798.

779 Lamber, EP, Guicheney, P, and Pinotsis, N (2022). The role of the M-band myomesin proteins in
780 muscle integrity and cardiac disease. J Biomed Sci 29, 18.

781 Lekes, D, Szadvari, I, Krizanova, O, Lopusna, K, Rezuchova, I, Novakova, M, Novakova, Z,
782 Parak, T, and Babula, P (2016). Nilotinib induces ER stress and cell death in H9c2 cells. Physiol
783 Res 65, S505–S514.

784 Lord, SJ, Velle, KB, Mullins, RD, and Fritz-Laylin, LK (2020). SuperPlots: Communicating
785 reproducibility and variability in cell biology. Journal of Cell Biology 219, e202001064.

786 Louch, WE, Koivumäki, JT, and Tavi, P (2015). Calcium signalling in developing
787 cardiomyocytes: implications for model systems and disease. J Physiol 593, 1047–1063.

788 Lundy, SD, Zhu, W-Z, Regnier, M, and Laflamme, MA (2013). Structural and Functional
789 Maturation of Cardiomyocytes Derived from Human Pluripotent Stem Cells. Stem Cells Dev 22,
790 1991–2002.

791 Luo, W, Lieu, ZZ, Manser, E, Bershadsky, AD, and Sheetz, MP (2016). Formin DAAM1
792 Organizes Actin Filaments in the Cytoplasmic Nodal Actin Network. PLoS One 11, e0163915.

793 McCain, ML, and Parker, KK (2011). Mechanotransduction: the role of mechanical stress,
794 myocyte shape, and cytoskeletal architecture on cardiac function. Pflugers Arch - Eur J Physiol
795 462, 89–104.

796 Ménard, C, Pupier, S, Mornet, D, Kitzmann, M, Nargeot, J, and Lory, P (1999). Modulation of
797 L-type calcium channel expression during retinoic acid- induced differentiation of H9C2 cardiac
798 cells. Journal of Biological Chemistry 274, 29063–29070.

799 Naito, AT, Shiojima, I, Akazawa, H, Hidaka, K, Morisaki, T, Kikuchi, A, and Komuro, I (2006).
800 Developmental stage-specific biphasic roles of Wnt/β-catenin signaling in cardiomyogenesis and
801 hematopoiesis. Proceedings of the National Academy of Sciences 103, 19812–19817.

802 Pahnke, A, Conant, G, Huyer, LD, Zhao, Y, Feric, N, and Radisic, M (2016). The role of Wnt
803 regulation in heart development, cardiac repair and disease: A tissue engineering perspective.
804 Biochemical and Biophysical Research Communications 473, 698–703.

805 Pradhan, L, Genis, C, Scone, P, Weinberg, EO, Kasahara, H, and Nam, H-J (2012). Crystal
806 Structure of the Human NKX2.5 Homeodomain in Complex with DNA Target. Biochemistry 51,
807 6312–6319.

808 Quaife-Ryan, GA, Mills, RJ, Lavers, G, Voges, HK, Vivien, CJ, Elliott, DA, Ramialison, M,
809 Hudson, JE, and Porrello, ER (2020). β-Catenin drives distinct transcriptional networks in
810 proliferative and nonproliferative cardiomyocytes. Development 147, dev193417.

811 Sardão, VA, Oliveira, PJ, Holy, J, Oliveira, CR, and Wallace, KB (2009). Morphological
812 alterations induced by doxorubicin on H9c2 myoblasts: nuclear, mitochondrial, and cytoskeletal
813 targets. Cell Biol Toxicol 25, 227–243.

814 Scarselli, M, Annibale, P, and Radenovic, A (2012). Cell Type-specific β2-Adrenergic Receptor
815 Clusters Identified Using Photoactivated Localization Microscopy Are Not Lipid Raft Related,
816 but Depend on Actin Cytoskeleton Integrity. J Biol Chem 287, 16768–16780.

817 Selmin, O, Thorne, PA, Caldwell, PT, Johnson, PD, and Runyan, RB (2005). Effects of
818 trichloroethylene and its metabolite trichloroacetic acid on the expression of vimentin in the rat
819 H9c2 cell line. Cell Biol Toxicol 21, 83–95.

820 Severs, NJ, Bruce, AF, Dupont, E, and Rothery, S (2008). Remodelling of gap junctions and
821 connexin expression in diseased myocardium. Cardiovasc Res 80, 9–19.

822 Shirai, YM, Tsunoyama, TA, Hiramoto-Yamaki, N, Hirosawa, KM, Shibata, ACE, Kondo, K,
823 Tsurumune, A, Ishidate, F, Kusumi, A, and Fujiwara, TK (2017). Cortical actin nodes: Their
824 dynamics and recruitment of podosomal proteins as revealed by super-resolution and single-
825 molecule microscopy. PLoS One 12, e0188778.

826 Suhaeri, M, Subbiah, R, Van, SY, Du, P, Kim, IG, Lee, K, and Park, K (2015). Cardiomyoblast
827 (H9c2) Differentiation on Tunable Extracellular Matrix Microenvironment. Tissue Eng Part A
828 21, 1940–1951.

829 Sun, Z, and Südhof, TC (2021). A simple Ca2+-imaging approach to neural network analyses in
830 cultured neurons. J Neurosci Methods 349, 109041.

831 Vandesompele, J, De Preter, K, Pattyn, F, Poppe, B, Van Roy, N, De Paepe, A, and Speleman, F
832 (2002). Accurate normalization of real-time quantitative RT-PCR data by geometric averaging of
833 multiple internal control genes. Genome Biol 3, research0034.1-0034.11.

834 Varela, R, Rauschert, I, Romanelli, G, Alberro, A, and Benech, JC (2021). Hyperglycemia and
835 hyperlipidemia can induce morphophysiological changes in rat cardiac cell line. Biochemistry
836 and Biophysics Reports 26, 100983.

837 van Veen, TAB, van Rijen, HVM, and Opthof, T (2001). Cardiac gap junction channels:
838 modulation of expression and channel properties. Cardiovascular Research 51, 217–229.

839 Watkins, SJ, Borthwick, GM, and Arthur, HM (2011). The H9C2 cell line and primary neonatal
840 cardiomyocyte cells show similar hypertrophic responses in vitro. In Vitro Cell Dev Biol Anim
841 47, 125–131.

842 Xia, S, Lim, YB, Zhang, Z, Wang, Y, Zhang, S, Lim, CT, Yim, EKF, and Kanchanawong, P
843 (2019). Nanoscale Architecture of the Cortical Actin Cytoskeleton in Embryonic Stem Cells.
844 Cell Reports 28, 1251-1267.e7.

845 Xu, X, Ruan, L, Tian, X, Pan, F, Yang, C, and Liu, G (2020). Calcium inhibitor inhibits high
846 glucose-induced hypertrophy of H9C2 cells. Mol Med Rep 22, 1783–1792.

847

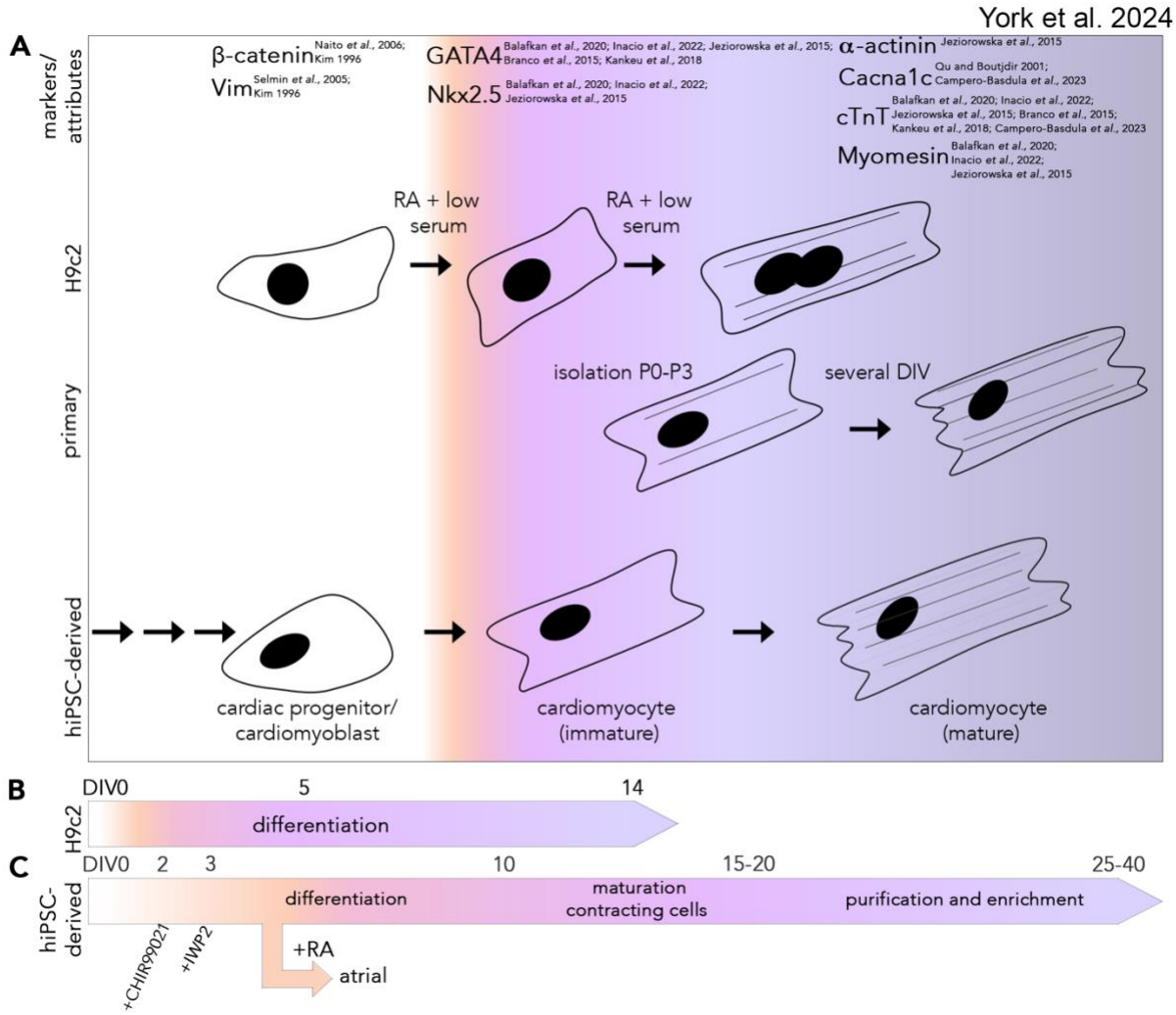

Figure 1. H9c2 cells display key markers of cardiomyocytes with a shorter culturing protocol compared to other models. (A) H9c2 cells undergo a variety of genetic changes during H9c2 cell differentiation, upregulating key cardiomyocyte genes and proteins such as *Cacna1c* ($Ca_v1.2$), *Tnnt2* (cTnT), and *Myom2* (Myomesin-2). In comparison to other models, H9c2 cells model cardiomyocyte differentiation whereas primary cardiomyocytes which isolate mature cells and are already cardiomyocyte fate determined and do not require the lengthy reprogramming and differentiation protocols that hiPSC-derived cardiomyocytes require. (B) H9c2 culturing protocols include the addition of low serum and ATRA to DIV14 (C) while hiPSC-CM culturing protocols require addition of multiple compounds over a longer culturing time.

York et al. 2024

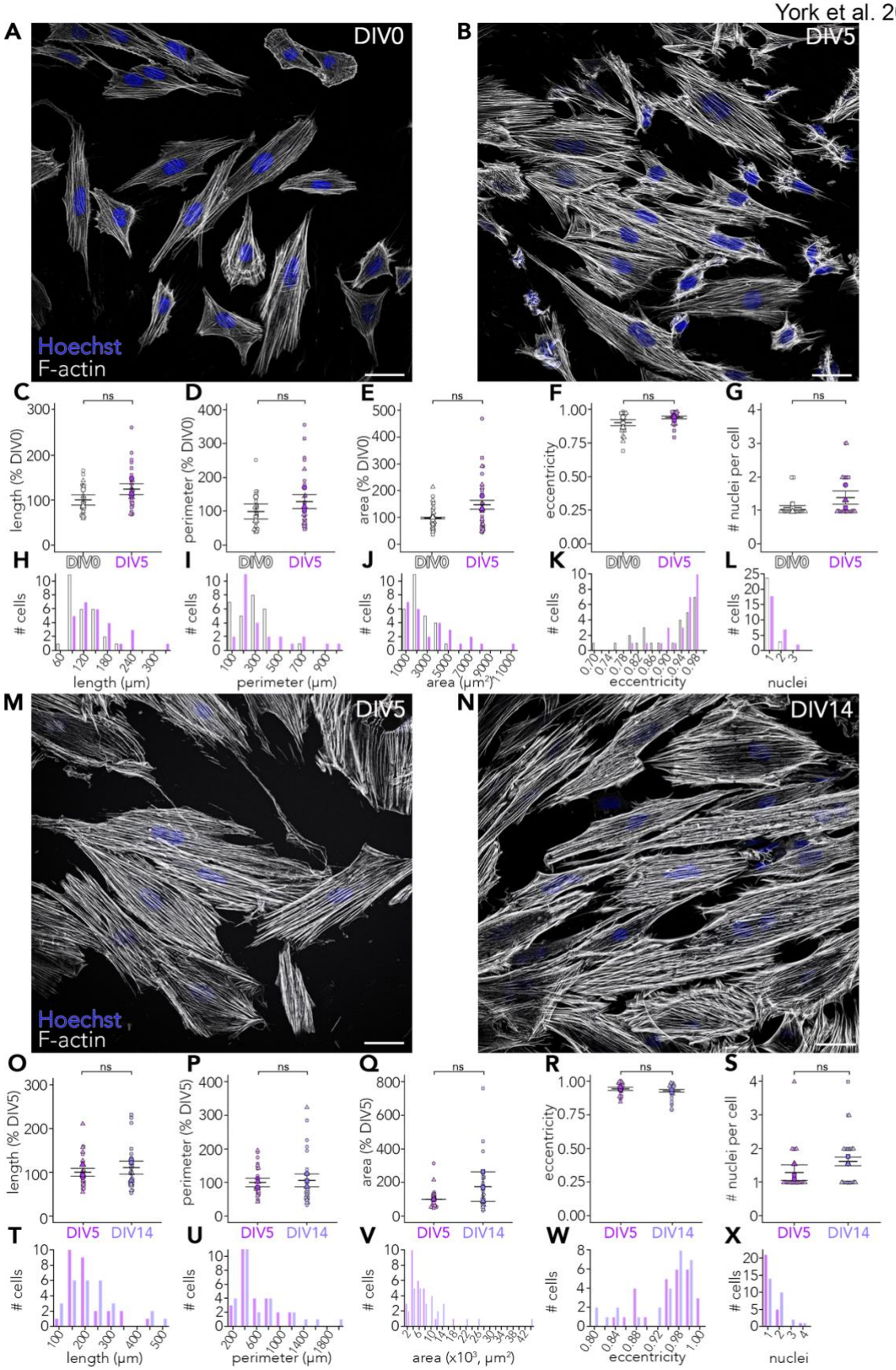

Figure 2. Subpopulations of differentiated H9c2 cells display increased length, perimeter, and number of nuclei at DIV5 and DIV14. H9c2 cell morphology at (A) DIV0 and (B) DIV5 was analyzed using the F-actin stain Phalloidin (white) and nuclei were counted via Hoechst staining (blue). Length, perimeter, area, eccentricity, and the number of nuclei per cell were measured using a custom MATLAB script which resulted in no significant increases in (C) length, (D) perimeter, (E) area, (F) eccentricity, or (G) number of nuclei per cell from DIV0 to DIV5. Density distribution plots show cell (H) length, (I) perimeter, and (J) area at DIV5 display larger values than at DIV0, (K) no major shifts in eccentricity, but increases in the (L) number of nuclei per cell. H9c2 cell morphology was then analyzed at (M) DIV5 and (N) DIV14. No significant changes were observed in (O) length, (P) perimeter, (Q) area, (R) eccentricity, or (S) number of nuclei per cell. The distribution of data between DIV5 and DIV14 is more similar for (T) length; however, (U) perimeter and (V) area all have higher measurements at DIV14 than at DIV5, at DIV14 the (W) eccentricity distribution is similar between DIVs while there is an increased (X) number of nuclei per cell. N = 3 replicates, n = 27 cells for all groups (3 cells from each of the 3 FOV were selected). (C-G, O-S) Data is presented as mean ± SEM and (H-L, T-X) density distribution plots display the spread of data. Results are graphed as White = DIV0, Purple = DIV5, Violet = DIV14. Scale bar = 40 μm. ns, $p > 0.05$ by Welch's t-test relative to control (C-G) DIV0 or (O-S) DIV5, see Table 1 for detailed statistics.

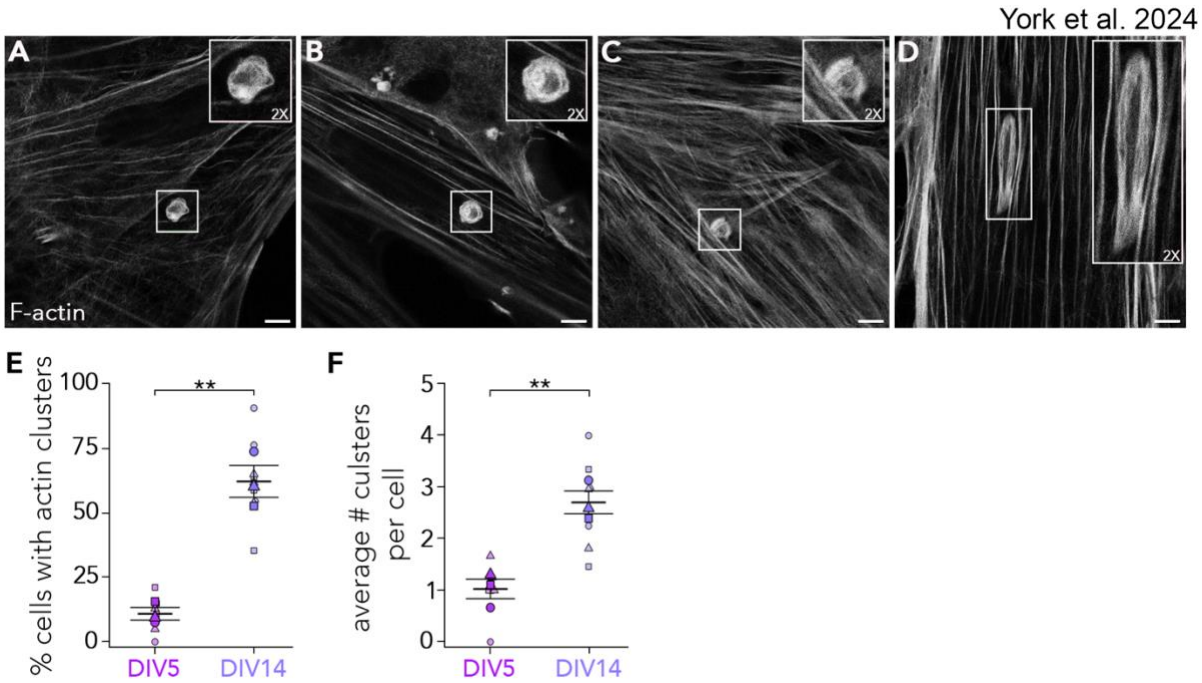

Figure 3. H9c2 cells display actin clusters at DIV14. STED imaging was performed to visualize the shape of the actin clusters visible at 20X (Figure 2 N). (A-C) Circular and (D) elliptical vortices were present in many of the cells. (E) Quantification of the percent of cells displaying actin clusters is higher at DIV14 than DIV5 (Welch's t-test, "**", p=0.0072). (F) The number of actin clusters per cell also is increased at DIV14 (Welch's t-test, "**", p=0.0048). N = 3 replicates, 3 FOV each. Data is presented as mean ± SEM. Scale bar = 5 µm, inlays were zoomed in by a factor of 2.

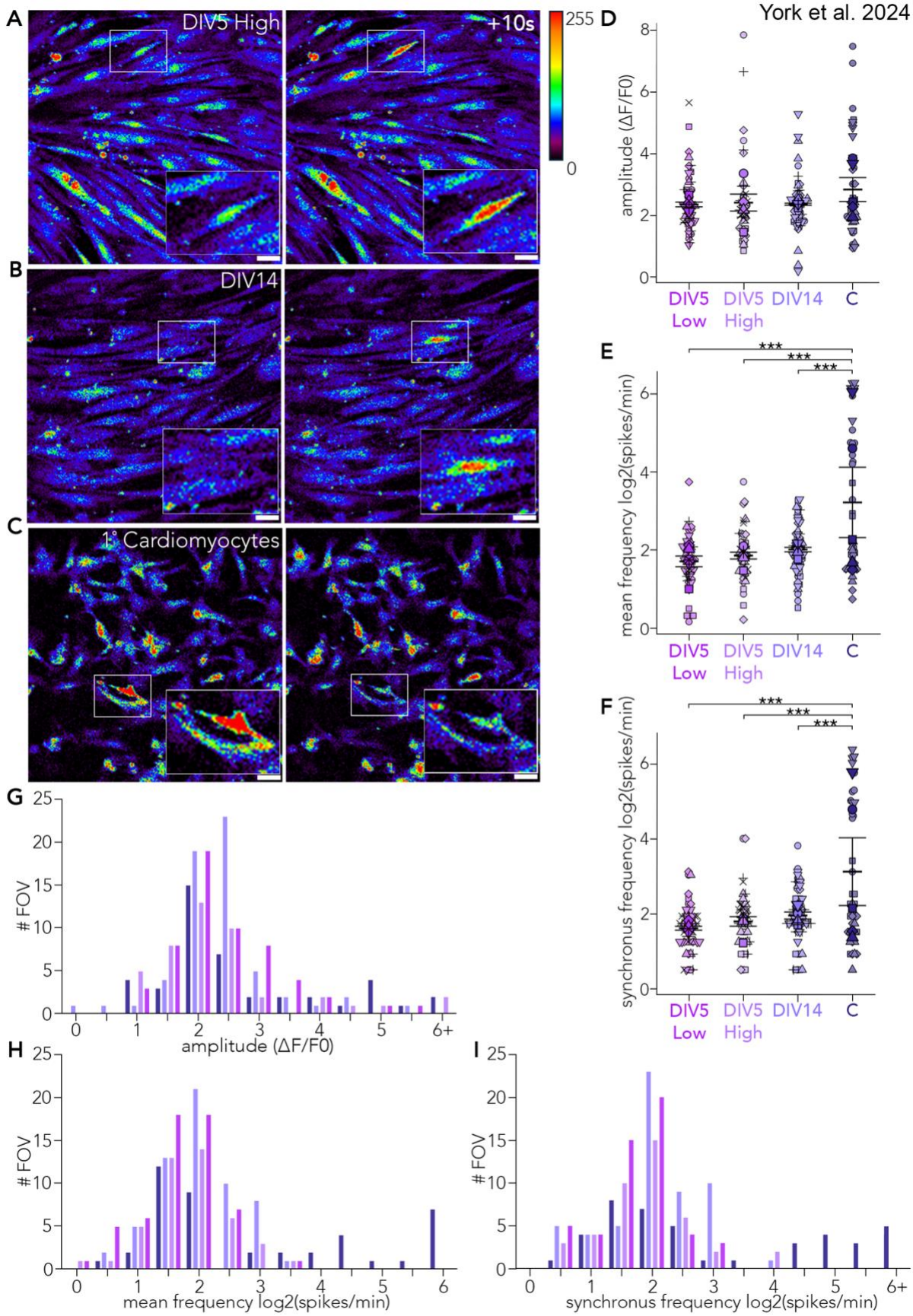
York et al. 2024
A
DIV5 High
+10s
255
0
B
DIV14
C
1° Cardiomyocytes
D
amplitude (ΔF/F0)
DIV5 Low
DIV5 High
DIV14
C
E
mean frequency log2(spikes/min)
***
F
synchronus frequency log2(spikes/min)
G
FOV
amplitude (ΔF/F0)
H
mean frequency log2(spikes/min)
I
synchronus frequency log2(spikes/min)

Figure 4. H9c2 cells undergo spontaneous changes in internal Ca^{2+}at DIV5 and DIV14 of which some subpopulations of DIV14 cells display transient frequencies and synchronicities approaching those seen in primary cardiomyocytes. Ca^{2+} imaging of differentiated H9c2 cells was performed using fluo-4 AM, cell permeant. Stills 10 seconds apart from 2 min (A) H9c2 DIV5 high, (B) H9c2 DIV14, or 1 min (C) primary cardiomyocytes time series show spontaneous changes in $[Ca^{2+}]_i$. Inlays highlight active cells in the field of view (FOV) undergoing a spike in $[Ca^{2+}]_i$. See supplemental Videos 1-4 for corresponding live imaging recordings. Superplots illustrate H9c2 cells have similar (D) spike amplitude to primary cardiomyocytes while (E) frequency and (F) synchronous firing rate are significantly different. Frequency distribution plots show the distribution of each group for (G) spike amplitude, (H) frequency, and (I) synchronous firing rate highlighting right shifts at DIV14 for (H) frequency and (I) synchronous firing rate. Primary cardiomyocytes (C; N = 5 replicates), DIV14 (N = 6 replicates), DIV5 1.0×10^4 cells/cm^2 (N = 6 replicates), DIV5 8.33×10^3 cells/cm^2 (N = 7 replicates). Data is presented as mean ± SEM. Results are graphed as Purple = DIV5 low, Lavender = DIV5 high, Violet = DIV14, Cobalt = C. Scale bar = 40 µm. ***, $p \leq 0.001$ by one-way ANOVA and *post-hoc* Dunnett's multiple comparison relative to primary cardiomyocytes, see Table 3 for detailed statistics.

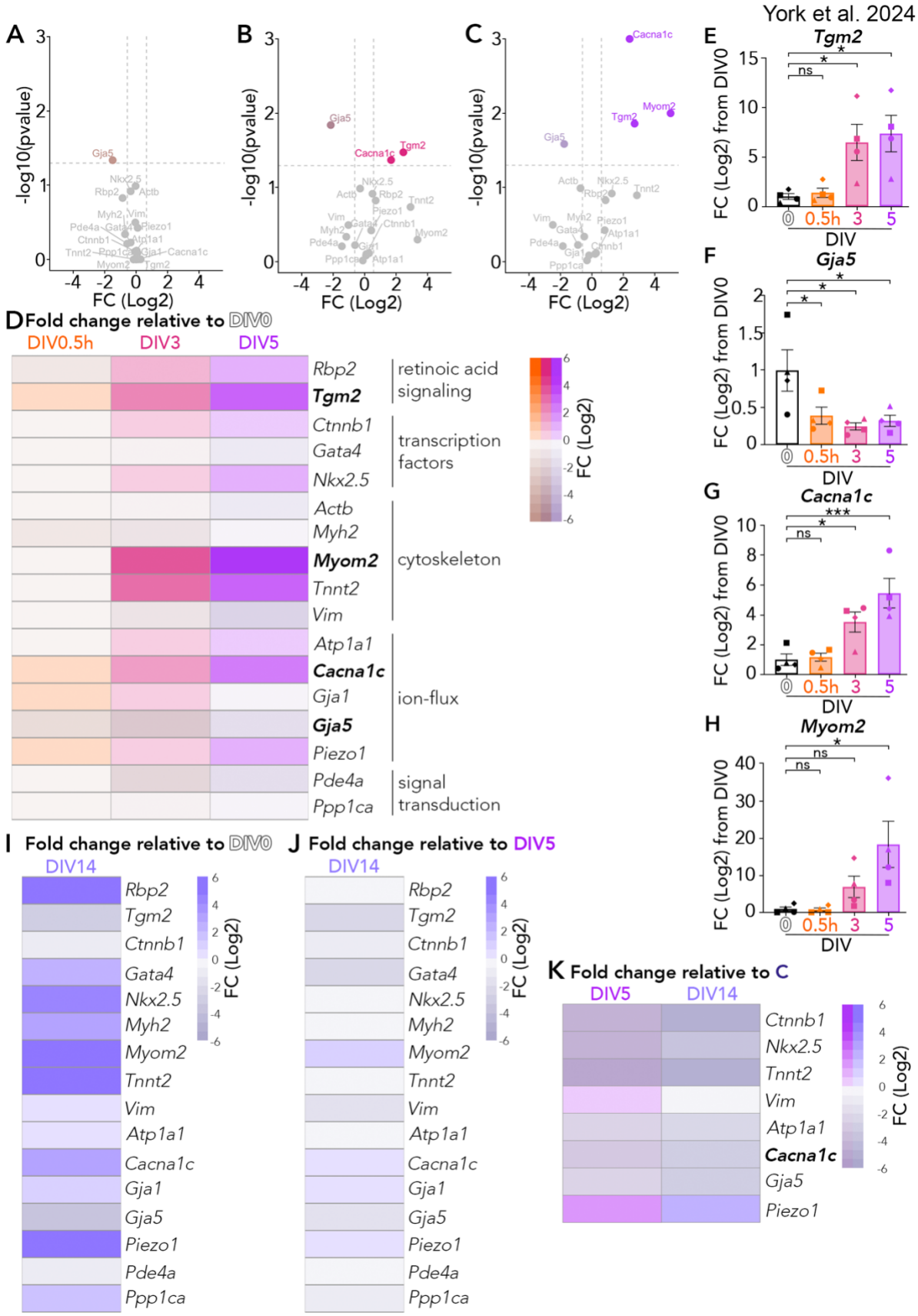
York et al. 2024
A
B
C
-log10(pvalue)
FC (Log2)
Gja5
Cacna1c
Tgm2
Myom2
D Fold change relative to DIV0
DIV0.5h
DIV3
DIV5
Rbp2
Tgm2
Ctnnb1
Gata4
Nkx2.5
Actb
Myh2
Myom2
Tnnt2
Vim
Atp1a1
Cacna1c
Gja1
Gja5
Piezo1
Pde4a
Ppp1ca
retinoic acid signaling
transcription factors
cytoskeleton
ion-flux
signal transduction
FC (Log2)
E
Tgm2
F
Gja5
G
Cacna1c
H
Myom2
FC (Log2) from DIV0
DIV
0.5h
ns
I Fold change relative to DIV0
DIV14
J Fold change relative to DIV5
K Fold change relative to C
DIV5
DIV14

Figure 5. H9c2 cell differentiation alters transcript expression levels of cardiomyocyte morphology markers and ion channels. Transcript levels of genes involved in retinoic acid signaling, transcription, cytoskeleton, ion flux regulation, and signal transduction were analyzed. (A-C) Volcano plots highlight 4 genes are differentially expressed during H9c2 cell differentiation. (D) Heatmap displaying log2 fold change (FC) relative to DIV0. Transcripts that had significant differences are bolded. (E) Over a short differentiation time course from DIV0 to DIV5, *Tgm2* levels were increased at DIV3 and DIV5 (confirming retinoic acid signaling). (F) *Gja5* underwent significant decreases starting at DIV0.5, and continuing to decrease at both DIV3 and DIV5. (G) *Cacna1c* levels increased at DIV3 and DIV5. (H) *Myom2* levels increased at DIV5. (I) Comparing DIV0 to DIV14 resulted in more pronounced changes. (J) From DIV5 to DIV14 there were no significant differences in transcript expression levels. (K) H9c2 cell transcript levels were also compared to primary cardiomyocytes in which only *Cacna1c* levels were significantly different at DIV5 but not DIV14. (A-H) DIV0, DIV0.5h, DIV3, DIV5 (N = 4); (J, K) DIV5, DIV14, primary cardiomyocytes (N = 3). ns, $p > 0.05$; *, $p \leq 0.05$ *; $p \leq 0.01$, ***; $p \leq 0.001$ by one-way ANOVA and *post-hoc* Dunnett's multiple comparison relative to primary cardiomyocytes, see Table 4 for detailed statistics.

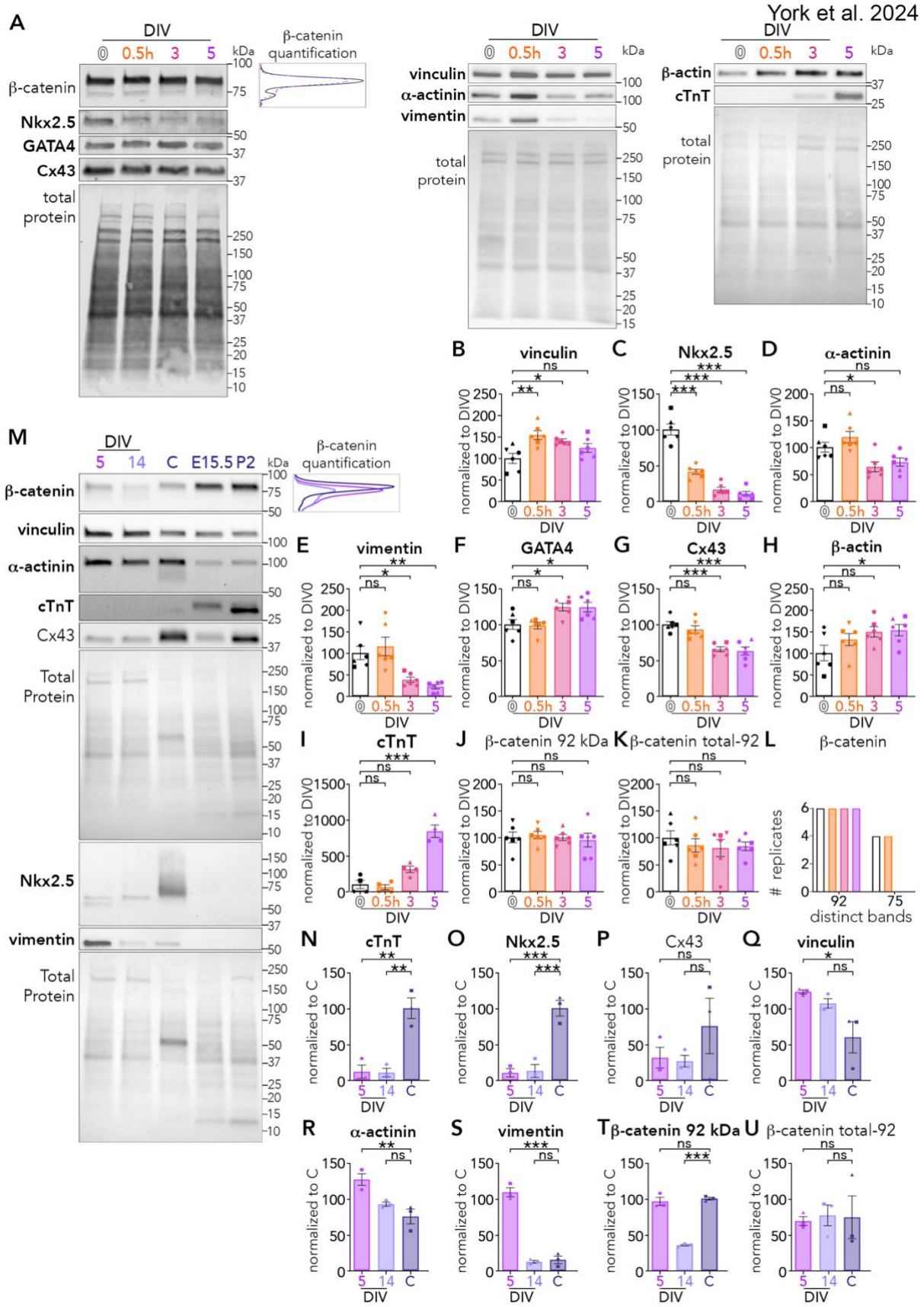
York et al. 2024
A
DIV
0 0.5h 3 5
kDa
β-catenin quantification
β-catenin
Nkx2.5
GATA4
Cx43
total protein
vinculin
α-actinin
vimentin
β-actin
cTnT
B vinculin
C Nkx2.5
D α-actinin
normalized to DIV0
M
5 14 C E15.5 P2
Total Protein
E vimentin
F GATA4
G Cx43
H β-actin
I cTnT
J β-catenin 92 kDa
K β-catenin total-92
L β-catenin
replicates
92 75
distinct bands
N cTnT
O Nkx2.5
P Cx43
Q vinculin
normalized to C
R α-actinin
S vimentin
T β-catenin 92 kDa
U β-catenin total-92

Figure 6. H9c2 cell differentiation alters protein expression levels of cardiomyocyte transcription factors and morphology markers. (A) Representative western blots from either Licor Odyssey CLx imager (first panel) or Syngene G:Box imager (second and third panel) and their associated total proteins were analyzed over a short differentiation time course from DIV0 to DIV5. The plot of the β-catenin quantification is included to shed light on the analytical process, Purple = DIV5, Violet = DIV14, Cobalt = C (primary cardiomyocytes). Graphs are displayed presenting proteins whose levels altered earliest (ie DIV0.5h). (B) Vinculin levels are increased at DIV0.5h and DIV3 while (C) Nkx2.5 levels decrease at DIV0.5h which is maintained to DIV5. (D) α-actinin levels decreased at DIV3 only while (E) vimentin levels are decreased at DIV3 and DIV5. (F) GATA4 levels were increased at DIV3 and DIV5. (G) Cx43 levels were decreased at DIV3 and DIV5. (H) β-actin and (I) cTnT levels were increased at DIV5. (J-L) the β-catenin profile displayed 2 bands at DIV0 which at DIV5 presented as a smear. (M) Representative western blots and their associated total proteins comparing DIV5, DIV14, primary cardiomyocytes, and mouse heart tissue from P2 and E15.5. The plot of the β-catenin quantification is included to shed light on the analytical process. Both (N) cTnT and (O) Nkx2.5 have significantly decreased levels compared to primary cardiomyocytes. (P) Cx43 levels were not significantly different between groups. (Q) Vinculin, (R) α-actinin, and (S) vimentin levels were significantly different from primary cardiomyocytes at DIV5 but not at DIV14. (T, U) The 92 kDa band of β-catenin was significantly different from primary cardiomyocytes at DIV14 but not at DIV5; however, the total signal-92 kDa was not significantly different between groups. DIV0, DIV0.5h, DIV3, DIV5 (N = 6, except cTnT N = 4); DIV14, primary cardiomyocytes, P2, E15.5 (N = 3). ns, $p > 0.05$; *, $p \leq 0.05$ *; $p \leq 0.01$, ***; $p \leq 0.001$ by one-way ANOVA and *post-hoc* Dunnett's multiple comparison relative to primary cardiomyocytes, see Table 5 for detailed statistics.

York et al. 2024

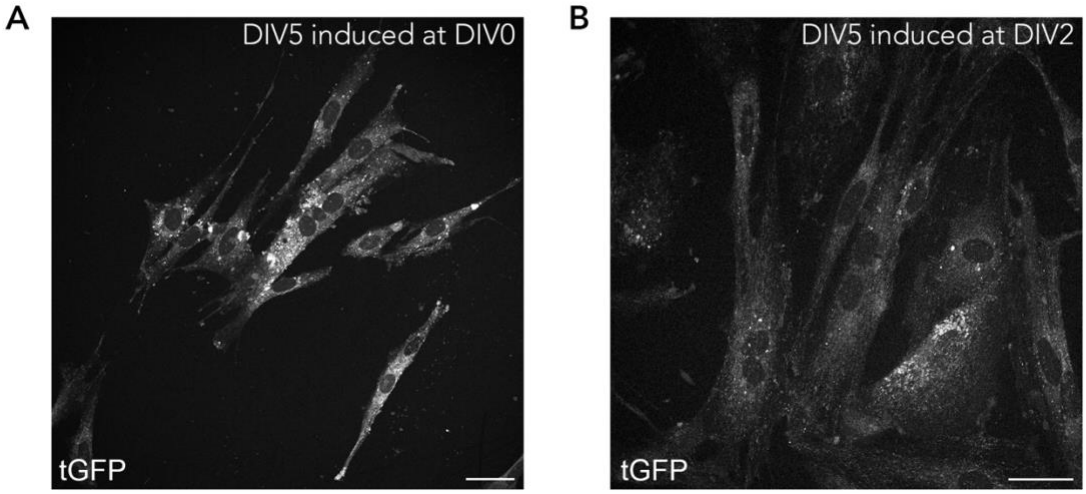

Figure 7. H9c2 cell transfection has a high transfection efficiency. H9c2 cells were seeded at 8.33 x 10^3 cells/cm^2 and transfected with the Tet-inducible GFP plasmid the next day. Either the following day at (A) DIV0 or at (B) DIV2 GFP expression was induced with the addition of doxycycline hyclate, cells were differentiated until DIV5. Representative images show how efficient H9c2 transfection with jetPEI can be for future researchers investigating the role of genetic variants. DIV0, DIV2 induced (N =3, 4 FOV each).

Table 1. Summary statistics of H9c2 cell morphology analysis results in no statistically significant changes from DIV0 to DIV5 or DIV5 to DIV14. Minimum (Min) and maximum (Max) values for each condition as well as the Mean ± SEM are listed. A student's t-test was performed and p values for each comparison are listed below the means. N=3 replicates with 4 FOV each.

Parameter	Timepoint	Min	Max	Mean ± SEM p-value
Normalized Length	DIV0	39.1 µm	215 µm	100% ± 11.4
	DIV5	46.7 µm	468 µm	124% ± 12.0 p=0.225
	DIV5	55.1 µm	210 µm	100% ± 8.89
	DIV14	52.6 µm	231 µm	111% ± 9.33 p=0.5738
Normalized Perimeter	DIV0	39.2 µm	252 µm	100% ± 22.2
	DIV5	47.8 µm	356 µm	130% ± 36.1 p=0.3875
	DIV5	42.7 µm	196 µm	100% ± 7.36
	DIV14	32.5 µm	324 µm	106% ± 11.1 p=0.6568
Normalized Area	DIV0	39.1 µm	215 µm	100% ± 2.92
	DIV5	46.7 µm	468 µm	149% ± 16.4 p=0.09154 "."
	DIV5	47.9 µm	314 µm	100% ± 0.21
	DIV14	32.7 µm	761 µm	175% ± 50.7 p=0.2758
Eccentricity	DIV0	0.7	0.99	0.91 ± 0.022
	DIV5	0.8	0.99	0.95 ± 0.01 p=0.2258
	DIV5	0.85	1	0.95 ± 0.007
	DIV14	0.79	0.99	0.93 ± 0.006 p=0.1831
Multinucleation	DIV0	1	2	1.11 ± 0.064
	DIV5	1	3	1.41 ± 0.196 p=0.2663
	DIV5	1	4	1.30 ± 0.134
	DIV14	1	4	1.63 ± 0.074 p=0.1135

Table 2. Summary statistics of H9c2 cell spontaneous calcium dynamics. Minimum (Min) and maximum (Max) values for each condition as well as the Mean ± SEM are listed for each parameter. Primary cardiomyocytes (N=5), DIV14 (N=6), DIV5 high (N=6), DIV5 low (N=7).

Parameter	Timepoint	Min	Max	Mean ± SEM
Average Amplitude	DIV5 low	1.04	5.67	2.36 ± 0.121
	DIV5 high	0.848	7.87	2.42 ± 0.209
	DIV14	0.191	5.30	2.36 ± 0.108
	1° Cardiomyocytes	0.936	7.50	2.80 ± 0.237
Average Frequency	DIV5 low	1.11	13.1	3.59 ± 0.246
	DIV5 high	1.16	13.1	4.03 ± 0.336
	DIV14	1.42	9.66	4.37 ± 0.255
	1° Cardiomyocytes	1.66	75.3	18.6 ± 3.68
Synchronicity Rate	DIV5 low	0.991	8.91	3.27 ± 0.232
	DIV5 high	0.495	16.3	4.09 ± 0.472
	DIV14	0.495	14.4	4.38 ± 0.324
	1° Cardiomyocytes	0.990	83.2	18.2 ± 3.53

Table 3. Statistics of H9c2 cell spontaneous calcium dynamics. A one-way ANOVA was performed, if this provided a significant result, then the Dunnett multiple comparisons test was used to determine which groups were significant. To compare DIV5 low and DIV5 high a Welch's t-test was performed. Primary cardiomyocytes (N=5), DIV14 (N=6), DIV5 high (N=6), DIV5 low (N=7).

Parameter	Comparison to C	p-value ANOVA	p-value Dunnett
Amplitude	DIV5 low	0.2007 "ns"	
	DIV5 high		
	DIV14		
Frequency	DIV5 low	<0.0001 "***"	<0.0001 "***"
	DIV5 high		<0.0001 "***"
	DIV14		<0.0001 "***"
Synchronicity Rate	DIV5 low	<0.0001 "***"	<0.0001 "***"
	DIV5 high		<0.0001 "***"
	DIV14		<0.0001 "***"
Parameter	Comparison to DIV5 low	Welch's t-test	
Amplitude	DIV5 high	0.7945 "ns"	
Frequency	DIV5 high	0.2618 "ns"	
Synchronicity Rate	DIV5 high	0.2142 "ns"	

Table 4. H9c2 cell transcript levels of key cardiomyocyte cytoskeletal proteins and ion channels increases over differentiation. For DIV5, which was compared to DIV0, and DIV5 and DIV14, which were compared to C, a one-way ANOVA was performed, if this provided a significant result, then the Dunnett multiple comparisons test was used to determine which groups were significant. DIV14 comparisons to DIV0 are listed; however, no statistical analysis can be performed as they were not from the same time course of experiments. For DIV14, which was compared to DIV5, a Welch's t-test was performed. DIV0, DIV0.5h, DIV3, DIV5 (N=4); DIV5, DIV14, primary cardiomyocytes (N=3).

Transcript	DIV	FC from DIV0	Log2	p-value ANOVA	p-value Dunnett
Rbp2	0.5h	0.68 ± 0.26	-0.90	0.148 "ns"	
	3	1.82 ± 0.48	0.73		
	5	2.04 ± 0.57	0.87		
	14	89.90 ± 39.20	5.86		
Tgm2	0.5h	1.38 ± 0.47	0.26	0.00819 "**"	0.9942 "ns"
	3	6.49 ± 3.66	2.49		0.0331 "*"
	5	7.38 ± 3.70	2.71		0.0138 "*"
	14	0.25 ± 0.16	-2.67		
Myh2	0.5h	0.71 ± 0.17	-0.74	0.456 "ns"	
	3	0.57 ± 0.20	-1.14		
	5	0.75 ± 0.13	-0.49		
	14	8.10 ± 2.33	2.87		
Tnnt2	0.5h	1.35 ± 0.59	-0.04	0.0943 "."	1.000 "ns"
	3	9.89 ± 3.68	2.95		0.181 "ns"
	5	10.90 ± 5.33	2.86		0.127 "ns"
	14	109.00 ± 57.50	5.93		
Ctnnb1	0.5h	0.97 ± 0.17	-0.11	0.78 "ns"	
	3	1.17 ± 0.25	0.14		
	5	1.17 ± 0.14	0.20		
	14	0.88 ± 0.61	-0.91		

Gata4	0.5h	0.79 ± 0.11	-0.39	0.591 "ns"	
	3	0.79 ± 0.24	-0.58		
	5	0.56 ± 0.08	-0.89		
	14	13.80 ± 9.01	2.59		
Nkx2.5	0.5h	1.18 ± 0.50	-0.39	0.12 "ns"	
	3	1.55 ± 0.30	0.53		
	5	2.60 ± 0.65	4.99		
	14	30.90 ± 12.70	4.46		
Actb	0.5h	0.96 ± 0.11	-0.08	0.102 "ns"	
	3	0.85 ± 0.10	-0.26		
	5	0.62 ± 0.07	-0.73		
Myom2	0.5h	0.83 ± 0.46	-0.20	0.0115 "*"	1.000 "ns"
	3	6.95 ± 2.88	3.39		0.499 "ns"
	5	18.40 ± 6.22	4.99		0.010 "*"
	14	28.40 ± 12.60	5.54		
Vim	0.5h	1.28 ± 0.52	-0.10	0.317 "ns"	
	3	0.65 ± 0.45	-1.00		
	5	0.32 ± 0.15	-2.48		
	14	1.14 ± 0.77	0.47		
Atp1a1	0.5h	1.07 ± 0.23	-0.01	0.76 "ns"	
	3	1.34 ± 0.29	0.31		
	5	1.28 ± 0.28	0.27		
	14	1.11 ± 0.27	0.05		
Cacna1c	0.5h	1.17 ± 0.39	0.08	0.00096 "***"	0.9953 "ns"
	3	3.54 ± 0.68	1.71		0.0421 "*"
	5	5.49 ± 1.0	2.39		<0.001 "***"
	14	7.60 ± 2.38	2.80		

Gja1	0.5h	1.04 ± 0.12	0.03	0.816 "ns"	
	3	1.10 ± 0.08	0.12		
	5	0.93 ± 0.18	-0.19		
	14	2.50 ± 0.74	1.21		
Gja5	0.5h	0.39 ± 0.12	-1.52	0.0201 "*"	0.0457 "*"
	3	0.25 ± 0.05	-2.12		0.0142 "*"
	5	0.32 ± 0.08	-1.76		0.0259 "*"
	14	0.11 ± 0.06	-3.70		
Peizo1	0.5h	1.17 ± 0.33	0.05	0.374 "ns"	
	3	1.53 ± 0.40	0.45		
	5	2.00 ± 0.58	0.81		
	14	35.80 ± 12.40	4.94		
Pde4a	0.5h	0.97 ± 0.55	-0.60	0.612 "ns"	
	3	0.46 ± 0.38	-1.42		
	5	0.36 ± 0.17	-1.85		
	14	0.64 ± 0.19	-0.76		
Ppp1ca	0.5h	0.99 ± 0.12	-0.05	0.952 "ns"	
	3	0.97 ± 0.15	-0.09		
	5	0.88 ± 0.19	-0.31		
	14	4.29 ± 1.66	1.74		

Transcript	DIV	FC from DIV5	Log2	p-value Welch's t-test
Rbp2	14	0.99 ± 0.43	-0.64	0.9883 "ns"
Tgm2	14	0.39 ± 0.24	-2.01	0.3658 "ns"
Ctnnb1	14	0.92 ± 0.63	-0.85	0.9273 "ns"
Gata4	14	0.38 ± 0.24	-2.62	0.5319 "ns"
Nkx2.5	14	0.98 ± 0.40	-0.53	0.9799 "ns"
Myh2	14	0.82 ± 0.24	-0.44	0.7179 "ns"
Myom2	14	1.98 ± 0.88	0.68	0.4148 "ns"

Tnnt2	14	1.22 ± 0.64	-0.56	0.7963 "ns"	
Vim	14	0.56 ± 0.37	-1.51	0.6210 "ns"	
Atp1a1	14	0.96 ± 0.23	-0.16	0.9063 "ns"	
Cacna1c	14	1.36 ± 0.43	0.32	0.5058 "ns"	
Gja1	14	1.24 ± 0.37	0.19	0.6073 "ns"	
Gja5	14	0.42 ± 0.24	-1.78	0.3723 "ns"	
Peizo1	14	1.44 ± 0.50	0.31	0.4944 "ns"	
Pde4a	14	0.79 ± 0.23	-0.45	0.5776 "ns"	
Ppp1ca	14	0.56 ± 0.22	-1.20	0.4843 "ns"	
Transcript	Group	FC from C	Log2	p-value ANOVA	p-value Dunnett
Tnnt2	DIV5	0.04 ± 0.02	-5.29	0.3477 "ns"	
	DIV14	0.05 ± 0.03	-5.06		
Ctnnb1	DIV5	0.06 ± 0.03	-4.63	0.0766 "ns"	
	DIV14	0.06 ± 0.04	-5.02		
Nkx2.5	DIV5	0.09 ± 0.07	-4.35	0.4234 "ns"	
	DIV14	0.09 ± 0.04	-3.94		
Vim	DIV5	1.89 ± 1.36	0.12	0.7560 "ns"	
	DIV14	1.05 ± 0.70	-0.59		
Atp1a1	DIV5	0.18 ± 0.03	-2.52	0.2100 "ns"	
	DIV14	0.18 ± 0.04	-2.61		
Cacna1c	DIV5	0.12 ± 0.03	-3.14	0.0445 "*"	0.0458 "*"
	DIV14	0.16 ± 0.05	-2.75		0.0551 "ns"
Gja5	DIV5	0.40 ± 0.20	-2.06	0.3337 "ns"	
	DIV14	0.17 ± 0.10	-3.09		
Peizo1	DIV5	4.12 ± 1.88	1.92	0.1131 "ns"	
	DIV14	5.92 ± 2.06	2.35		

Table 5. H9c2 cell protein levels of key cardiomyocyte cytoskeletal proteins and cardiac markers increases over differentiation. A one-way ANOVA was performed, if this provided a significant result, then the Dunnett multiple comparisons test was used to determine which groups were significant. For DIV14, which was compared to DIV5, a Welch's t-test was performed. DIV0, DIV0.5h, DIV3, DIV5 (N=6, except cTnT N=4); DIV5, DIV14, primary cardiomyocytes (N=3).

Protein	DIV	Normalized Percent to DIV0	p-value ANOVA	p-value Dunnett
β-catenin	0.5h	99% ± 5.13	0.986 "ns"	
	3	100% ± 4.49		
	5	103% ± 10.5		
Nkx2.5	0.5h	41.3% ± 3.36	<0.001 "***"	<0.001 "***"
	3	16.6% ± 3.32		<0.001 "***"
	5	10.9% ± 3.09		<0.001 "***"
GATA4	0.5h	98.5% ± 4.51	0.00435 "**"	0.9958 "ns"
	3	124% ± 5.31		0.0225 "*"
	5	124% ± 6.60		0.0234 "*"
α-actinin	0.5h	119% ± 9.16	0.00134 "**"	0.3594 "ns"
	3	63.5% ± 10.5		0.0284 "*"
	5	72.3 ± 7.60		0.1111 "ns"
Cx43	0.5h	92.9% ± 5.26	<0.001 "***"	0.5855 "ns"
	3	65.6% ± 3.39		<0.001 "***"
	5	63.1% ± 5.71		<0.001 "***"
cTnT	0.5h	61.3% ± 35.2	<0.001 "***"	0.9389 "ns"
	3	311% ± 44.9		0.0692 "ns"
	5	839% ± 87.2		<0.001 "***"
vinculin	0.5h	154% ± 10.2	0.00429 "**"	0.0017 "**"
	3	141% ± 4.58		0.0180 "*"
	5	124% ± 10.0		0.1981 "ns"
vimentin	0.5h	115% ± 21.5	<0.001 "***"	0.7823 "ns"
	3	38.0% ± 6.00		0.0128 "*"
	5	21.9% ± 4.76		0.0019 "**"

β-actin	0.5h	131% ± 14.0	0.0663 "ns"	0.3174 "ns"
	3	149% ± 11.9		0.0654 "ns"
	5	153% ± 13.1		0.0447 "*"
Protein	DIV	Normalized Percent to DIV5	p-value Welch's t-test	
β-catenin 92 kDa	14	36.7% ± 0.9	0.0019 "**"	
β-catenin total-92 kDa	14	107% ± 13.2	0.7777 "ns"	
Nkx2.5	14	125% ± 85.3	0.8197 "ns"	
α-actinin	14	73.7% ± 8.3	0.0667 "ns"	
Cx43	14	78.0% ± 12.6	0.1605 "ns"	
cTnT	14	276% ± 214	0.4972 "ns"	
vinculin	14	87.9% ± 14.4	0.5141 "ns"	
vimentin	14	11.4% ± 1.9	<0.0007 "***"	
Protein	Group	Normalized Percent to C	p-value ANOVA	p-value Dunnett
β-catenin 92 kDa	DIV5	96.2 % ± 5.6	<0.0001 "***"	0.6800 "ns"
	DIV14	35.3% ± 1.1		<0.0001 "***"
β-catenin total-92	DIV5	92.9% ± 8.3	0.9571 "ns"	
	DIV14	104% ± 19.5		
Nkx2.5	DIV5	10.3% ± 5.7	0.0005 "***"	0.0006 "***"
	DIV14	12.9% ± 8.9		0.0007 "***"
α-actinin	DIV5	169% ± 10.7	0.0085 "**"	0.0057 "**"
	DIV14	123% ± 4.0		0.2726 "ns"
Cx43	DIV5	41.5% ± 19.1	0.3558 "ns"	
	DIV14	35.2% ± 10.6		
cTnT	DIV5	11.9 % ± 9.2	0.0013 "**"	0.0017 "**"
	DIV14	10.7% ± 5.9		0.0016 "**"
vinculin	DIV5	205% ± 4.5	0.0352 "*"	0.0263 "*"
	DIV14	178% ± 11.0		0.0789 "ns"

vimentin	DIV5	725% ± 42.0	<0.0001 "***"	<0.0001 "***"
	DIV14	82.5% ± 13.4		0.9002 "ns"

Table 6. RT-qPCR assay panel for characterizing cardiomyocyte gene expression.

Gene	PrimeTime qPCR probe assay code	Fluorophore	Category
Rbp2	Rn.PT.58.38085782	Cy5	retinoic acid signaling
Tgm2	Rn.PT.58.13093079	Cy5	
Ctnnb1	Mm.PT.58.10078649	Cy5	transcription Factors
GATA4	Mm.PT.58.30024990	Fam	
Nkx2.5	Rn.PT.58.11528139	Fam	
Actb	Mm.PT.39a.22214843.g	Fam	cytoskeleton
Actn1	Mm.PT.58.30787926	Hex	
Myh2	Mm.PT.58.7469087	Cy5	
Myom2	Rn.PT.58.10611775	Hex	
Tnnt2	Mm.PT.58.12681437	Hex	
Vim	Mm.PT.58.8720419	Fam	
Atp1a1	Rn.PT.58.17975975	Fam	ion-flux
Cacna1c	Rn.PT.58.16361922	Hex	
GJA1	Rn.PT.58.10553710	Cy5	
GJA5	Rn.PT.58.7544937	Fam	
Piezo1	Rn.PT.58.46120084	Cy5	
Pde4a	Rn.PT.58.6046707	Cy5	signal transduction
Ppp1ca	Mm.PT.58.23629119	Hex	
Polr2a	Mm.PT.39a.22214849	Cy5	housekeeping
Ppia	Mm.PT.39a.2.gs	Fam	

Table 7. Western blot targets for characterizing cardiac protein expression.

Antibody	Company, Catalog	Concentration	Category
α-actinin	Cell Signalling Technology, 3134S	1:1000	Cardiac-specific Markers
cTnT	Abcam, ab10214	1:2000	
β-catenin	Cell Signalling Technology, 37477	1:500, 1:1500	Cardiac Transcription Factor
GATA4	Santa Cruz Biotechnology, sc-25310	1:25	
Nkx2.5	Abcam, ab97355	1:400	
β-actin	Sigma, A5441	1:2000	Cytoskeleton
Vinculin	Sigma, MAB3574	1:60000, 1:10000	
Vimentin	Cell Signalling Technology, 5741	1:80000	
Connexin43	Cell Signalling Technology, 3512	1:500	Ion Fluxes
Peroxidase-Affinipure Donkey Anti-Mouse IGG (H+L)	Jackson Immuno Research, 715-035-150	1:8000	Peroxidase Secondaries
Peroxidase-Affinipure Donkey Anti-Rabbit IGG (H+L)	Jackson Immuno Research, 711-035-152		
IRDye 800CW Donkey anti-Rabbit IgG (H + L)	Li-cor, 926-32213	1:8000	Fluorescent Secondaries
IRDye 680RD Donkey anti-Mouse IgG (H + L)	Li-cor, 926-68072		
IRDye 800CW Donkey anti Mouse IgG (H + L)	Li-cor, 926-32212		
IRDye® 680RD Donkey anti-Rabbit IgG (H+L)	Li-cor, 926-68073		